Nanoscale

REVIEW

Multifunctional composite core–shell nanoparticles

Suying Wei,[a] **Qiang Wang,**[b] **Jiahua Zhu,**[c] **Luyi Sun,**[d] **Hongfei Lin**[e] **and Zhanhu Guo**[*c]

In this review paper, the state-of-the-art knowledge of the core–shell multifunctional nanoparticles (MNPs), especially with unique physiochemical properties, is presented. The synthesis methods were summarized from the aspects of both the advantages and the demerits. The core includes the inexpensive and easily oxidized metals and the noble shells include the relatively noble metals, carbon, silica, other oxides, and polymers. The properties including magnetic, optical, anti-corrosion and the surface chemistry of the NPs are thoroughly reviewed. The current status of the applications is reviewed with the detailed examples including the catalysis, giant magnetoresistance (GMR) sensing, electromagnetic interface shielding or microwave absorption, biomedical drug delivery, and the environmental remediation.

[a]*Department of Chemistry and Biochemistry, Lamar University, Beaumont, TX, 77710, USA*

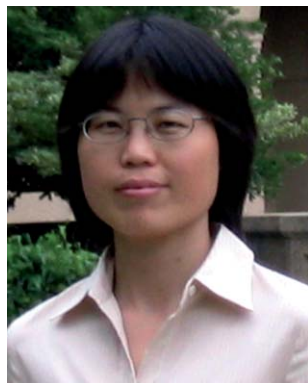[b]*Department of Chemistry, University of Oxford, Mansfield Road, Oxford, OX1 3TA, UK*

[c]*Integrated Composites Laboratory (ICL), Dan F. Smith Department of Chemical Engineering, Lamar University, Beaumont, TX, 77710, USA. E-mail: Zhanhu.guo@lamar.edu; Fax: +1 (409) 880-2197; Tel: +1 (409) 880-7654*

[d]*Department of Chemistry and Biochemistry & Materials Science and Engineering Program, Texas State University-San Marcos, San Marcos, TX, 78666, USA*

[e]*Chemical and Materials Engineering Department, University of Nevada, Reno, NV, 89557, USA*

1. Introduction

Nanoparticles (NPs) from transition iron-group metals such as iron,[1–5] cobalt[5–17] and nickel[2,5,18–25] are of great interest due to their unusual physicochemical properties such as enhanced magnetic moment[26] and enlarged coercivity[1,27] arising from their tiny size less than 100 nm and high specific surface area (ratio of the surface to the mass/volume). Compared with the bulk counterparts, these iron-group metal NPs have promising practical applications such as catalysts for growing carbon nanotubes (CNTs)/carbon fibers[28–34] and carbon–carbon bonds,[35–39] ultrahigh density magnetic recording media,[40–44] magnetic fluids,[45–47]

Suying Wei

Dr Suying Wei, currently an Assistant Professor in the Department of Chemistry and Biochemistry at Lamar University, obtained a PhD degree in chemistry from Louisiana State University (2006), a MS in applied chemistry from Beijing University of Chemical Technology (2000) and BS in chemical engineering from Shandong University of Science and Technology (1996). Her research interests are in multifunctional composites especially those towards biomedical applications. Her expertise is in analytical, materials and surface chemistry. She was awarded NSF summer institute fellowship, Pfizer graduate fellowship and Robinson award for excellent research in analytical science during previous professional development.

Qiang Wang

*Dr Qiang Wang is currently a postdoctoral associate in the University of Oxford. He received his BSc (2003) and MSc (2005) from Harbin Institute of Technology (HIT) in China, and his PhD (2009) from Pohang University of Science and Technology (POSTECH) in South Korea. Before moving to Oxford, he had worked in the Institute of Chemical and Engineering Sciences (ICES) under A*STAR, Singapore for two years. His research interests are heterogeneous catalysis and materials chemistry, with a particular focus on energy and environmental issues. He was awarded the Chinese Government Award for Outstanding Self-Financed Students Abroad in 2008.*

structural polymer nanocomposites (PNCs)[48–56] and biomedical drug delivery.[57] Additionally, iron-group metal NPs have been synthesized as alloys either within the iron-group elements[58–72] or with other metals such as Au,[73] Pd,[74,75] Pt,[76–80] Ru(Rh),[81] Cu,[82] and C,[83–87] which broaden the potential applications of these iron-group metal NPs.

The potential applications of these metallic iron-group NPs are limited due to their propensity to be easily oxidized in air or moisture and fast dissolution under acidic conditions. The easy and rapid oxidation/dissolution of the NPs is due to the large specific surface area inherent with the small size. In order to address this challenge, several approaches have been investigated. The most widely reported approach, albeit not easily achieved, is to coat the iron-group metal cores with a protective shell, which includes noble metals, carbon, silicon oxide (silica),

zirconia (ZrO_2) and polymers. The iron-group oxides are also known to be utilized as shell materials leading to favorable magnetic core–shell particles to protect them from further oxidation. The reported iron-group NPs with a protective shell include carbon coated Co,[88–98] Ni[92,93,95,97–104] and Fe,[56,92,93,105–108] silica coated Co,[109–113] Fe,[114,115] Fe_3O_4,[116] and Fe–Ni alloy,[117] NiO coated Ni,[103,118] ZrO_2 coated Fe,[119] iron oxide coated Fe,[120,121] Au coated Fe/Co,[122–130] platinum,[131] palladium,[132,133] copper,[134] alumina,[64] yttria (Y_2O_3),[65] or silver[135,136] coated iron-group metal NPs. Polymers such as polyisobutylene functionalized with tetraethylenepentamine (PIB–TEPA) as a 1 : 1 mixture with mineral oils have also been reported to coat the Fe NPs.[137] Recently, semiconductor shells such as CdSe surrounding Co NPs were also reported.[138] Most importantly, the core–shell structure not only provides a stabilized magnetic property and

Jiahua Zhu

Mr Jiahua Zhu received his MS in Chemical Engineering from Nanjing University of Technology in 2009, where he researched self-lubricating sealing composite materials in the laboratory of Prof. Xiaohua Lu and Prof. Xin Feng. He is currently a PhD candidate with Prof. Zhanhu Guo in the Integrated Composites Laboratory (ICL) at Lamar University. His research interests involve new synthetic routes to multifunctional polymer nanocomposites with advanced applications in environmental remediation and micro-electronics such as giant magnetoresistance sensor and developing new nano-structured metacomposites based on conductive polymers incorporating different nanostructures, metal oxides, etc.

Hongfei Lin

Dr Hongfei Lin is an Assistant Professor in the Chemical and Materials Engineering Department at the University of Nevada, Reno. His current research activities focus on coupling chemical processes with novel material systems for renewable energy and clean fuel production. He received his B.E. and M.S. degrees in Chemical Engineering from Tsinghua University, China, in 1996 and 2000, respectively, and his PhD degree in Chemical Engineering from Louisiana State University, Baton Rouge in 2005. After graduation, he became a postdoctoral fellow for two years at the University of California, Santa Barbara and then worked in industry for three years.

Luyi Sun

Dr Luyi Sun is an Assistant Professor in the Department of Chemistry and Biochemistry at Texas State University-San Marcos. He received his PhD degree in chemistry at The University of Alabama in 2004 (mentored by Dr Joseph S. Thrasher). Following that, he did two years of postdoctoral research at Texas A&M University under the supervision of Profs. Abraham Clearfield and Hung-Jue Sue. From 2006 to 2009, he was a Senior Research Engineer at TOTAL Petrochemicals USA, Inc. Dr Sun's current research focuses on design and synthesis of nano-structured multifunctional materials for various applications.

Zhanhu Guo

Dr Zhanhu Guo, currently an Assistant Professor in Dan F. Smith Department of Chemical Engineering at Lamar University, obtained a PhD degree in Chemical Engineering from Louisiana State University (2005) and received a three-year (2005–2008) postdoctoral training in Mechanical and Aerospace Engineering Department in University of California Los Angeles. Dr Guo directs the Integrated Composites Laboratory and chairs the Composite Division of American Institute of Chemical Engineers (AIChE, 2010–2011). His current research focuses on multifunctional light-weight nanocomposites especially with polymer and carbon as the hosting matrix.

oxidative resistance but also broadens their potential applications such as optical–electronic devices and biomedical areas[124] since the shell can be functionalized with organic or biomolecular materials. The protective layer has also been applied in catalytic areas. For example, expensive metal Pd shell around a cheap Ni metal core results in cost-effective materials in catalysis.[132]

Though there are a couple of comprehensive reviews on the inorganic NP syntheses, in which most of the reported methods are summarized,[139,140] the reviews focusing on the core–shell NPs,[141] especially on the magnetic core nonmagnetic shell structural composite NPs, have rarely been reported. In this review paper, an up-to-date review of the fabrication techniques to prepare a protective shell around the iron-group metallic NPs is presented followed by a discussion on how these core–shell NPs are characterized. The effects of the protective shell on their properties will also be included and detailed information on the applications of these structural composite NPs will be documented. More specifically, three types of protective shells such as noble metal, insulator/metal oxide, and polymer are discussed in more detail. Due to the wide applications of the polymer shell, a separate section rather than being included in the insulator session is devoted to the preparation of polymer shells. However, the synthesis of monometallic iron-group NPs is not included as this part has already been extensively covered in the literature.[10,68,93,103,142–146] Although there are more applications for the magnetic core and nonmagnetic shell NPs in the coming future, the authors point out that the illustrated applications are limited due to the short history of the magnetic core and nonmagnetic shell NPs.

2. Methodologies for shell synthesis

Several methods have been developed to fabricate a protective shell around iron-group magnetic NPs and can be broadly classified into two categories: bottom-up and top-down. The bottom-up approaches can be further segmented into three classes: (i) simultaneous fabrication, where both the core and the protective shell formation takes place simultaneously; (ii) sequential fabrication, where the core is fabricated followed by the formation of a protective shell, and (iii) displacement reaction (redox) fabrication, wherein the protective shell is fabricated through the displacement of surface atoms of the metal core.

The simultaneous fabrication approach has mainly been adopted in the cases of carbon and silicon oxide (silica) coated metal nanoparticle fabrication. Sequential fabrication involves the initial formation of the iron-group metal cores followed by the formation of the desired shell without sacrificing the iron-group metal cores. This method is suitable for all the reported core–shell structural composite nanoparticle systems regardless of the iron-group metal core stability. The existing iron-group metal core will act as the nucleation sites (seeds) for the subsequent formed shell metal atoms to nucleate and grow up, such as in the reverse micelle and thermo-decomposition methods, or act as the substrate for the subsequent material to deposit, forming the shell. The displacement fabrication approach involves a redox reaction between the iron-group metal core and the desired precursor shell ions depending on the potential difference between the metal core and the metal shell. The displacement method is only suitable for the metal shell, which is nobler than

the iron-group metal core and can be performed either in organic or in aqueous media without additional reducing agent.

In addition to these common developed core–shell synthetic methods, there are other approaches under development. For example, segregation of the metastable binary metal composites can lead to the formation of core–shell NPs, such as Fe–Mg core–shell NPs.[144] In this review, the fabrication of different shell materials around the iron-group metal core will be discussed based on the aforementioned generalized fabrication categories.

2.1 Fabrication of noble metal shell

Introduction of a noble metal shell onto the magnetic metallic NPs is extremely attractive based on the stability of the core–shell structure and the wide potential applications. Among the reported methods to introduce the noble metallic shells, the reverse micelle method employing the simultaneous fabrication approach is well established, in which the micelles act as nanoreactors for the particle growth and the particle size can be easily controlled by adjusting the micelle size and the ratio of the reducing agent to the metal salt. This method is illustrated with the fabrication of a protective Au shell around Fe and Co NPs.[123,125,126,128,147,148] The fabrication can be briefly described as follows. Firstly, microemulsions from individual components are separately prepared. The metallic core is prepared by mixing the microemulsions containing the core metal ions and a reducing agent. To this mixture, the microemulsion with the shell metal ions is introduced simultaneously along with the required further additional reducing agent microemulsion. Once the reaction is completed, the core–shell particles are obtained by allowing the particles to settle down and washing off the excessive surfactant. This approach was reported to be utilized for the fabrication of Au shell around Fe core NPs and the oxidative stability of the Fe core was tested by X-ray spectroscopy (XAS) later.[123] This method has been extensively applied in Au or Ag shell formation around Co or Fe NPs. The incomplete coating of the magnetic core is an issue of this method. In addition, many pure shell metal NPs without the iron-group metal core are observed, which is another disadvantage of this method.

Thermal decomposition of the organometallic complexes is another widely adopted method for the shell fabrication. The formation of the core–shell structured composite NPs in this method is based on the faster core formation rate than that of the shell at the beginning of the reaction by choosing the suitable reaction condition. Thermo-decomposition of the organometallic salts in a coordinating solvent has also been utilized to obtain the shell around the core.[127,132] Here, the detailed synthetic information for the Ni–Pd core–shell NP synthesis is provided to depict the critical parameter, temperature, in the shell-controlled formation. The metal–trioctylphosphine (TOP) complex solution, which was prepared from the reaction of 1 : 1 (molar ratio) $Pd(acac)_2$ and $Ni(acac)_2$ in trioctylphosphine, was injected into oleylamine at various temperatures.[132] The Ni–TOP complex is found to get decomposed more easily than the Pd–TOP complex at a lower temperature and Pd–TOP is more easily decomposed than the Ni–TOP complex at a higher temperature. Based on this fact, the Ni cores can be formed firstly at a lower injecting temperature such as 205 °C for sufficient time to completely decompose the Ni–TOP complex, where the Pd–TOP rarely gets

decomposed, then increase the temperature to 235 °C to introduce the Pd shell around the Ni core.[132] While with the sequential decomposition method, the reversed core–shell NPs such as Pt–Co core–shell NPs are also fabricated with the increased temperature 205 °C for the decomposition of Pt–TOP and then the low temperature 142 °C for the decomposition formation of the Co shell.[149] Both systems are based on the same principle that the organometallic salts have different decomposition temperatures. In addition, the Co shell can be transformed into a hollow CoO structure, which will expose the Pd cores for serving as a catalyst.[150,151]

A third generalized approach for the fabrication of noble metal shell around iron-group metal cores is the displacement reaction. Compared with the sequential method, the displacement reaction method is based on the potential difference by sacrificing part of the core metal without any additional reducing agent. The displacement reaction has been employed to synthesize Co–Pt core–shell NPs in the neutral organic solution.[131] The stringent requirement here is that the Co precursor NPs should not be oxidized in order for the subsequently complete coating of the noble metal surrounding the Co NPs. The coating is achieved through sacrificing the surface iron-group core metal. However, the very reactive and easily oxidized iron-group metal NPs make the complete coating very difficult and is normally achieved in an inert condition.

The displacement reaction in fabricating the core–shell NPs has been further developed in Co–Cu NPs,[134] in which an acidic aqueous electrolyte solution was used rather than the neutral organic solution.[152] This method overcomes the neutral organic solution's limitation of the partially oxidized surface by introducing the acidic aqueous solution. The iron-group metal oxides on the nanoparticle surface easily react with the protons in the aqueous electrolyte and then the exposed NPs continue to react with the noble metal shell ions, which will deposit on the iron-group metal surface to prevent them from further reaction. This method has the potential to be used in other noble metal coating systems.
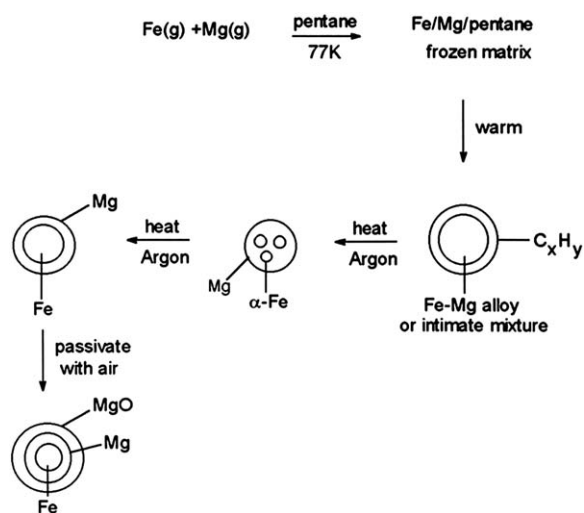
The fourth generalized approach for the shell preparation is not very commonly adopted and is normally applicable in situations like metastable alloys serving as the starting materials. The principle is based on the segregation of the metastable alloyed materials under high temperature annealing conditions to form core–shell NPs due to the immiscibility of the two metals such as Fe and Mg.[144] The metastable Mg–Fe composites formed by vapor deposition were heated at temperatures above 250 °C to segregate Mg and Fe. The scheme for the core–shell formation is shown in Fig. 1. No core–shell formation was observed when the heating temperature was below 250 °C. The formation of Fe–Mg core–shell NPs was tentatively explained from the point of thermodynamic effect under the heating condition, *i.e.* the Fe–Fe bonds are stronger than Mg–Mg or Fe–Mg bonds, which will favor the formation of the Mg shell around the iron core NPs. This method is also applicable to the Fe–Li system. However, it was reported that it didn't work in the Fe–Ag system. The Mg shell around Fe NPs has the advantage of serving as a sacrificial metal when the apparatus has trace oxygen to form a protective MgO coating, which could be a good shell for the Fe core NPs.[144]

The fifth generalized approach for the shell preparation is to create a gap between the core and the shell. This gap is composed of some layers of polymers, which interact with core structures through hydrophobic interactions, and combined with Au through an Au–S bond.[153] Before synthesizing the core–shell structure, Fe_3O_4 NPs were first capped with oleylamine and oleic acid through the thermal decomposition of iron(III) oleate in a mixture of oleylamine and oleic acid. The synthesis then starts with room temperature coating of Au on the surface of Fe_3O_4 nanoparticles by reducing $HAuCl_4$ in a chloroform solution of oleylamine. The Au-coated Fe_3O_4 nanoparticles are then transferred into water by mixing them with sodium citrate and cetyltrimethylammonium bromide (CTAB). The water-soluble core/shell Fe_3O_4/Au nanoparticles serve as seeds for the formation of Fe_3O_4/Au nanoparticles with thicker Au coating by simply adding more $HAuCl_4$ in the reducing condition or for the preparation of Fe_3O_4/Au/Ag nanoparticles by adding $AgNO_3$ to the reaction mixture. The control on the shell thickness allows the tuning of plasmonic properties of the core/shell nanoparticles to be either red-shifted (to 560 nm) or blue-shifted (to 501 nm). The significant contribution of the synthesis is that it offers not only a composite nanoparticle system with controlled magnetic and plasmonic properties but also a noble metal-coated surface for long-term stabilization of the magnetic core and nanoparticle functionalization. Such multifunctional nanoparticles should have great potentials for nanoparticle-based diagnostic and therapeutic applications.[153]

Comparing the above five reported methods, the demerits for the sequential formation method are the incomplete coating of the core and the formation of pure shell metal NPs. The displacement method is more advantageous than the other methods, in that it provides a complete coating and its facile operation; the demerit is that it will reduce the core size by sacrificing the core with the shell metal ions. The thermodecomposition method including the segregation of the metastable alloyed system (fourth method) is not easily controlled in the pure metal core and shell structure. The fifth approach provides a method for composite nanoparticle systems. The suitable method should be valued on the applications.

Fig. 1 Scheme of Fe–Mg core–shell nanoparticle formation from metastable alloys. (Reprinted with permission from American Chemical Society.)[144]

2.2 Fabrication of insulating silica and carbon shell

Insulating silica and semiconductive amorphous carbon have been reported as shell materials in protecting the magnetic metallic NPs from oxidation/dissolution. These core–shell structures can be easily bound with the biological materials through the surface physical adsorption or chemical bonding. The carbon coated magnetic NPs are normally synthesized by a chemical vapor deposition (CVD) method using the vaporization of the metal and carbon, which were deposited onto a substrate. The shell is formed by annealing, utilizing its immiscibility. The silica shell is normally formed by the wet chemical method. Iron-group NPs protected by the insulating shells have potential applications in magnetic data storage, ferrofluids, and contrast agents in magnetic resonance imaging.[88,96,98] The Kratschemer carbon arc process (standard arc method) has been used in the synthesis of the carbon shell combining metal NPs.[88,96,154,155] Briefly, the standard arc method is to bury the selected metals or metal oxide powders inside the drilled hole of the graphite anode. And at high temperatures, the metal core particles obtained from metal vapor are coated by carbon to form the carbon encapsulated metal NPs. The obtained carbon shell coated metallic NPs resist the etching by acids. The disadvantage of this method is that the yield of the carbon encapsulated metal particles is much lower than that of the other carbon products including carbon nanotubes (CNT), nanopowders, graphite flakes, and metal carbides. In addition, the control over the particle size and size distribution is a challenge. It is also difficult to obtain the pure and uncontaminated ferromagnetic transition metal cores. In order to overcome these drawbacks, a modified arc discharge method has been developed and the experimental set-up used is schematically illustrated in Fig. 2. The experimental set-up consists of an arc chamber with a vertical graphite rod cathode and an anode composed of a metal block such as nickel or other iron-group metals placed inside a graphite crucible. The transverse helium gas flow provides a quenching of the metal vapor during the arc plasma process. The metal block forms a melted pool and carbon is
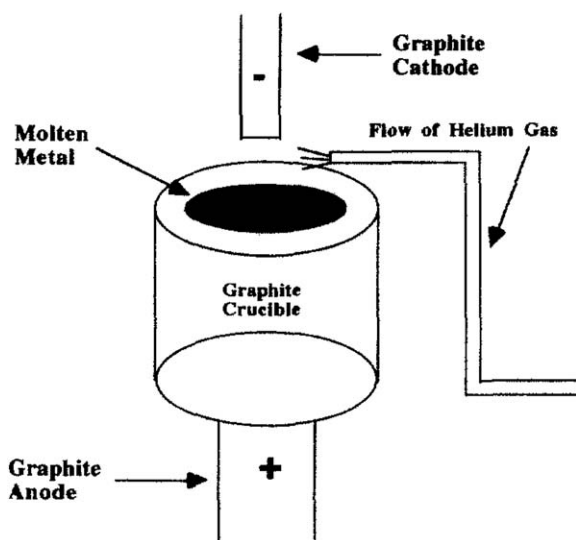
formed from the sputtering on the surrounding graphite crucible and the foil. The sputtered carbon enables the condensed metal clusters to be encapsulated completely. With this modified arc discharge method, the core–shell NPs are devoid of any impurities such as CNTs, graphitic flakes or coarse particles and the uncoated particles can be easily removed by the acid bath washing. The modified method has a major advantage that it is suitable for large-scale synthesis of metal NPs encapsulated with carbon.

The yield of the carbon coated metal NPs is dependent on the metal species and also critically on the operating conditions such as the geometry of the graphite crucible–metal anode assembly, like the inner diameter of the crucible.[87,104] The post-treatments of the carbon-coated iron-group metal, such as annealing, increase the graphite shell thickness, which is likely to arise from the increase of the graphitization of the coated carbon. The annealing temperature is chosen depending on the metal elements utilized for the shell growth. An added advantage of the high-temperature annealing process is that it can even change the carbon structure to multiwalled graphite shells and may lead, if the temperature is high enough, to the migration of the metal core out of the carbon shell and leave an empty graphitic shell.[87]

In comparison with the physical chemical methods used for the fabrication of carbon shell surrounding the ferromagnetic metal core NPs, a wet chemical synthetic method has also been developed for the fabrication of silica or alumina shells. The calcination of the shell and the reduction of the core are the typical procedures in forming core–shell structured composite NPs. Briefly, after preparing the organic (alcohol) ferromagnetic metal (single or mixed element) salt solution with controlled pH and temperature to form composites in solution, the composite powders were obtained by high temperature evaporation of the solvent. The silica coated ferromagnetic metal NPs were formed by calcination of the powders under the reducing agent to obtain the zero-valence ferromagnetic metal cores.[114,117] The valence state of the ferromagnetic metal core strongly depends on the subsequent calcination temperature. For the Co core, the optimum temperature is 1173 K for zero-valence Co-silica core–shell NPs, while at temperatures below 1073 K, the obtained NPs are onion-like structures with the Co_3O_4, CoO and fcc Co and amorphous silica subsequently from the inner core to the shell.

In addition, aluminium oxide (alumina) was introduced as a protecting shell material by the dehydration and further thermal reduction method.[64] Yttria was also coated onto the FeCo magnetic NPs by the thermal reduction of oxyhydroxide precursors.[65] The Fe–Co NPs (Co–goethite) were synthesized by sequential oxidation–precipitation of $FeSO_4$ and $Co(NO_3)_3$ solutions (0.1 M total salt concentration) with NaOH (0.35 OH/(Fe + Co) equivalent ratio) and then with Na_2CO_3 (1.5 CO_3^{2-}/(Fe + Co) equivalent ratio) at 40 °C.[65] The alumina coating was done by first dissolving the $Al(NO_3)_3$ (10^{-2} M) in 100 mL water followed by adding a 10% NaOH aqueous solution to reach a pH of 12.5. Then the Co–goethite NPs (1.0 g) were homogeneously suspended in the solution and CO_2 gas was bubbled into the slurry to lower the pH to 8.5 so that a hydrated aluminium oxide layer was deposited onto the surface of the particles. The initial pH was set to 12.5 in favor of the stabilization of the suspension due to the high density of the surface charge on the goethite particles. For the coating process, the particle surface remains
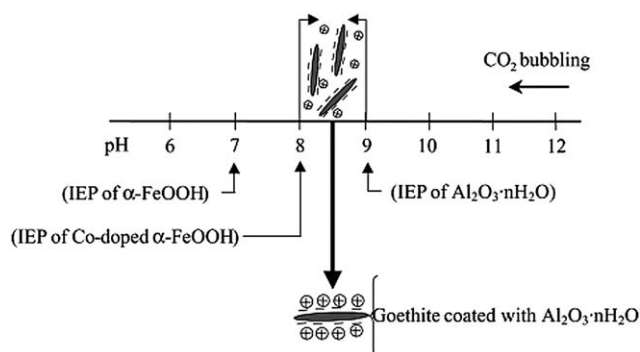

Fig. 2 A schematic diagram of the modified arc discharge chamber. (Reprinted with permission from American Institute of Physics.)[87]

Fig. 3 Scheme of the coating process. (Reprinted with permission from American Chemical Society.)[64]
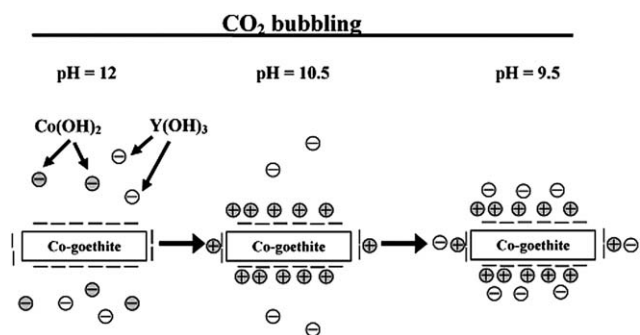

Fig. 4 Scheme of the coating process. (Reprinted with permission from American Chemical Society.)[65]

negative at a pH of 8.5, while the surface of the aluminium hydroxide nuclei is positively charged, favoring the homogeneous coating by the hetero-coagulation process (electrostatically induced coagulation of particles having opposite charge density). The scheme of the heterocoagulation process is shown in Fig. 3. In addition, the initial concentration of the $Al(NO_3)_3$ has an effect on the homogeneity of the coating, the optimum concentration is about 10^{-2} M. Higher concentration leads to the formation of the separate aluminium hydroxide particles, whereas lower concentration leads to the coating of the particles.[64] The Y_2O_3 coating was achieved by dissolving $Co(NO_3)_2$ and $Y(NO_3)_3$ at a pH of 3 in the nitrogen degassed water to prevent the oxidation of the Co(II) ions followed by adding KOH to a pH of ~12. Then the above Co–goethite NPs (10 g L^{-1}) were homogeneously suspended in the above solution. CO_2 gas was bubbled into the slurry immediately to lower the pH to a value of 10.5 and kept for 15 minutes, and then to a pH of 9.5. The specific pH value was chosen based on the different values of surface charge density at selected pH regions of the Co–goethite particles and the generated Co and Y species in the solution.[65] The coating scheme is shown in Fig. 4. After obtaining the above NPs, the dehydration was done at higher temperature, 400 °C for yttria and 600 °C for alumina. Then the NPs were reduced at 450 °C with a hydrogen flow of 40 L h^{-1}. The reduction temperature has an effect on the porosity of the particles.[65] Porosity in the yttria coating NPs is lower than the alumina coating due to the higher temperature treatment.

Compared with the noble metal shell formation, the used method for the insulator shell is rarely reported and is mainly focused on the wet chemical method such as for the above alumina and silica. The used adsorption method is complicated to control the coating while introducing the shell materials.

2.3 Fabrication of metallic oxide shell

Metallic oxide shells, especially the iron-group metal oxides around the magnetic metallic core, can form an exchange coupling, which can have an important positive impact on the magnetic properties. The normally used method is to control the content of the oxygen or air while exposing the NPs to passivate the zero-valence metal NPs.

The existence of an antiferromagnetic (AFM) shell such as CoO, FeO, and NiO around the ferromagnetic (FM) core can form the exchange-coupling interaction, leading to an increased blocking temperature (T_b)[156] and an enhanced coercivity (H_c).[157] This AFM shell provides some advantages to the naked zero-valence metal NPs such as stabilized and the improved magnetic properties. Here, it is necessary to mention how to fabricate the iron-group metal oxide shell around the iron-group metal core. The normal "bottom-up" method such as the gas condensation method[25,158,159] is to synthesize the iron-group metal NPs and then expose the NPs to the introduced gas, mixture of inert gas and oxygen/air.[1,118] The oxide coated magnetic NPs have great potential to be used in the giant magnetoresistance (GMR)/ tunnel magnetoresistance (TMR) sensors with enhanced magnetic properties, which will be discussed in the following.

2.4 Fabrication of polymeric shell

As compared with the other shell materials, a polymer shell has the following advantages: (1) it can serve as a surfactant or stabilizer to prevent the agglomeration of NPs; (2) it can be used to fabricate the nanocapsulation through the layer-by-layer method; and (3) it can be compatible with or functionalized with other materials by selectively choosing the shell materials such as branched poly(ethylenimine) shell around the poly(methyl methacrylate) (PMMA) core.

Polyisobutylene functionalized with tetraethylenepentamine (PIB–TEPA) as a 1 : 1 mixture with mineral oils was reported to coat the Fe NPs.[137] The formation route is schematically illustrated in Fig. 5. The NPs were synthesized by the thermal decomposition of iron pentacarbonyl ($Fe(CO)_5$) in the presence of ammonia and polymeric dispersants. $Fe(CO)_5$, PIB–TEPA, and kerosene mixture was degassed with argon for 20 minutes and then bubbled with ammonia for 20 minutes followed by increasing the temperature to 95 °C and keeping at this temperature for 8 hours. Then the solution temperature was increased to 190 °C and held for 2 hours. The reaction mixture was bubbled with ammonia and stirred throughout the reaction. The cooled magnetic NPs were precipitated by adding the reactant solution to a mixture of acetone and methanol. Purification of the NPs was done by the following two precipitations, one from hexane into acetone/methanol and the second time from hexane into pure acetone. Then it was isolated and dissolved in hexane and a rotary evaporator was used to remove hexane, and the remaining product was dried under vacuum condition with heating at 95 °C. With the modification of the process, other types of polymeric dispersants such as
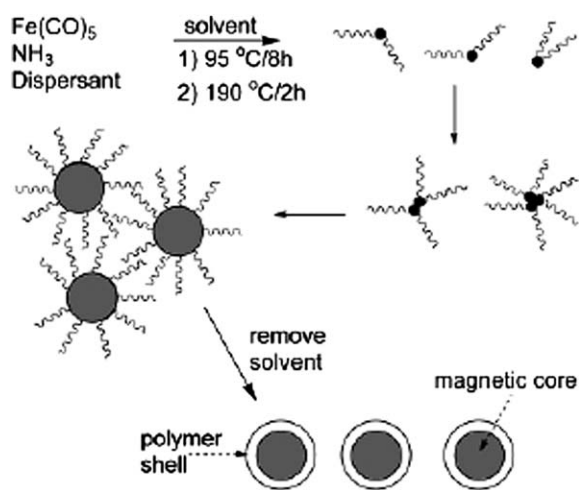
Fig. 5 Scheme of the polymer shell by the thermal decomposition method. (Reprinted with permission from American Chemical Society.)[137]

poly(ethylene-*graft*-tetraethylenepentamine maleimide) could also be employed for the coating of the magnetic NPs.

Except for the aforementioned method to coat the magnetic NPs with polymers, solvent-free atom transfer radical polymerization (ATRP) was also used to coat the magnetic NPs. Here, the synthesis of Fe_2O_3–polystyrene (PS) core–shell NPs is described as a typical example. The obtained oleic acid stabilized Fe_2O_3 NPs ($\sim$10 nm in diameter) dispersed in 2-bromo-2-methylpropionic acid (Br-MPA) hexane solution were stirred for 72 hours at room temperature under argon protection. The resulting powders were separated using a centrifuge and washed with hexane. This washing process was repeated one more time to remove the excess initiators. The Br-MPA functionalized NPs were dried under vacuum and then mixed with styrene monomer to form a transparent reddish solution for the ATRP reaction. The mixture was transferred into a flask with CuBr and 2,2-dipyridyl after purging with argon for 10 minutes. The reaction was conducted at 120 °C for 20 hours under stirring and nitrogen protection conditions. After the reaction was completed, the mixture was diluted with tetrahydrofuran (THF) at a solution/THF volume ratio of 1 : 10 and the final products were precipitated with methanol. The PS stabilized core–shell NPs were separated with the centrifuge and dissolved in toluene solution. This method has the potential to be applied to other nanoparticle systems for coating iron oxide NPs with increasing complexity and more functional polymeric shells.[160]

3. Physicochemical properties of the core–shell nanoparticles

Nanoparticles, defined by their size, are in the range of 1 to 100 nm. The classical physical laws no longer hold for this small size system. In strong chemical bonding materials, delocalization of the valence electrons will change dramatically with the change of the system size. This effect, combined with structural changes, could result in different chemical and physical properties from those of the bulk counterparts. The reported size-dependent properties include magnetic properties, optical properties,

melting heats, specific heats, and surface reactivity.[161] Due to the large specific surface area, the interaction between the surface and the core components will be predominant than that inside of the pure core NPs. For applications and technical studies, it is requisite to understand the intrinsic properties of the core–shell structure. The effectiveness of the shell in the prevention of the iron-group metal core from oxidizing in air and from dissolving in acid environments is an important factor in the practical biological and other applications. Also, the physical and chemical properties of the core–shell NPs will determine the application of these multifunctional materials.

3.1 Optical properties

The optical property is dependent on the material type, shell thickness and core size. Here, two cases are illustrated. The first case depicts the effects of the polymer shell on the optical property of the iron oxides (Fe_2O_3 and Fe_3O_4) and the second provides the core effect on the Au shell. The inter-particle separation was reported to affect the surface plasmon band shape and the peak position.[162] The plasmon resonance of the metal nanoshell is tunable by the ratio of the core radius and the thickness of the shell such as in the Au coated Au_2S NPs.[163]

The optical property was changed, normally dampened by the existence of the shell materials. The observed PS–Fe_2O_3 core–shell NPs were compared with the oleic acid stabilized Fe_2O_3 NPs by UV/vis spectrometer. Fig. 6(a) shows the UV/vis spectra of the oleic acid stabilized Fe_2O_3 NPs before (dotted line) and after (solid line) ligand exchange with Br-MPA. Fig. 6(b) shows UV/vis absorption spectra of PS–Fe_2O_3 core–shell NPs. The broad adsorption peaks at $\sim$470 nm were from Fe_2O_3. The yellowish core–shell nanoparticle toluene solution (figure inset) shows a weak absorption peak around 470 nm. The existence of the shell is justified to dampen the optical absorption.[160]

The optical properties of iron oxides can also be tuned by controlling the particle size and the assembly of the NPs. For instance, by assembling uniform superparamagnetic colloidal particles into 1D chain-like arrays in various liquid media, a novel magnetic tunable photonic structure can be developed.[164–170] The dynamic ordering of the magnetic colloids with controllable periodicity along the direction of the external field renders the system a fast, fully reversible photonic response across the visible near-infrared spectrum. The magnetic alignment of the chains and the corresponding photonic response can be observed using an optical microscope operated in the dark-field mode, Fig. 7. Without the influence of a magnetic field, no uniform colors can be observed due to the randomly dispersed chains in solution. When a vertical magnetic field is applied, all the chains are aligned along the field direction and appear as brightly colored dots. All the photonic chains within one sample show a single color due to the periodically arranged particles. The periodicity can be changed by varying the size of Fe_3O_4 colloidal nanocrystal clusters (CNCs). Photonic chains assembled from large CNCs (*ca.* 182 nm in diameter) diffract red light, while those from medium-sized particles (*ca.* 160 nm) diffract green light and those from small CNCs (*ca.* 113 nm) tend to diffract blue light, Fig. 7. It is reported that these optically active magnetic nanochains may find great applications in biological and chemical sensing and biomedical labeling and imaging.[171–175]
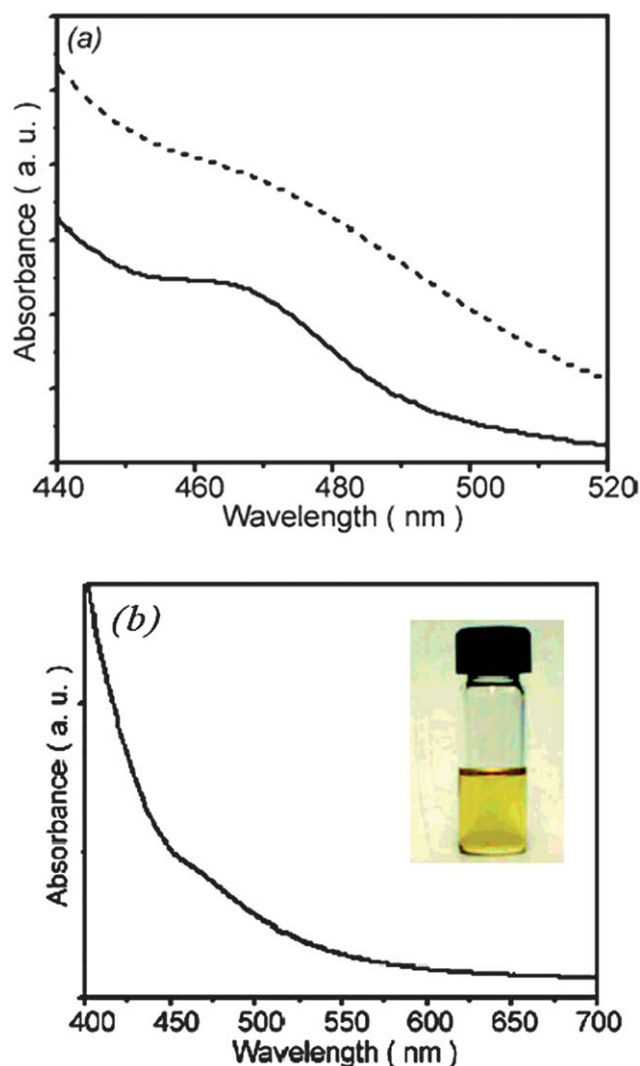
Fig. 6 UV/vis spectra of (a) oleic acid stabilized Fe$_2$O$_3$ NPs before (dotted lines) and after (solid lines) ligand exchange with Br-MPa and (b) PS–Fe$_2$O$_3$ core–shell NP toluene solution. (Reprinted with permission from American Chemical Society.)[160]

Fig. 7 Dark-field optical microscopy images of the magnetic photonic chains with different diffraction colors switched between "off" (a, c, e: without magnetic field) and "on" (b, d, f: with vertical magnetic field) states. These photonic chains diffract at different wavelengths because they were prepared using Fe$_3$O$_4$ CNCs of different average sizes: (a and b) 182 nm, (c and d) 160 nm, (e and f) 113 nm. All images are at the same scale. (Reprinted with permission from John Wiley and Sons.)[164]

The introduced noble metal shell around the magnetic NPs also has an effect on the UV/vis absorption. The γ-Fe$_2$O$_3$ NPs synthesized from the high temperature organic solution and the subsequent Au shells formed by the colloidal microemulsion technique were reported to demonstrate different optical properties as compared with that of the bare gold NPs.[176] The observed UV/vis absorption peak at around 572 nm (Au component ∼30.2 at% based on pure Au and Fe) shifts from the typical absorption wavelength of 525 nm for 10 nm Au NPs, which can be attributed to the variation in size, shape or agglomeration of the Au NPs. And the gold shell thickness has an effect on the optical property, the observed resonance peak shift to 552 nm, when the gold coating is reduced to ∼18 at% (EDS analysis).[176] Recently, a tailored synthesis of superparamagnetic Au nanoshells with tunable optical properties was reported by Zhang et al.[177] The particles are composed of a superparamagnetic Fe$_3$O$_4$ core, an Au nanoshell, and a mesoporous silica outer layer. The unique porous silica layer was utilized to control the seeded growth of Au NPs to form
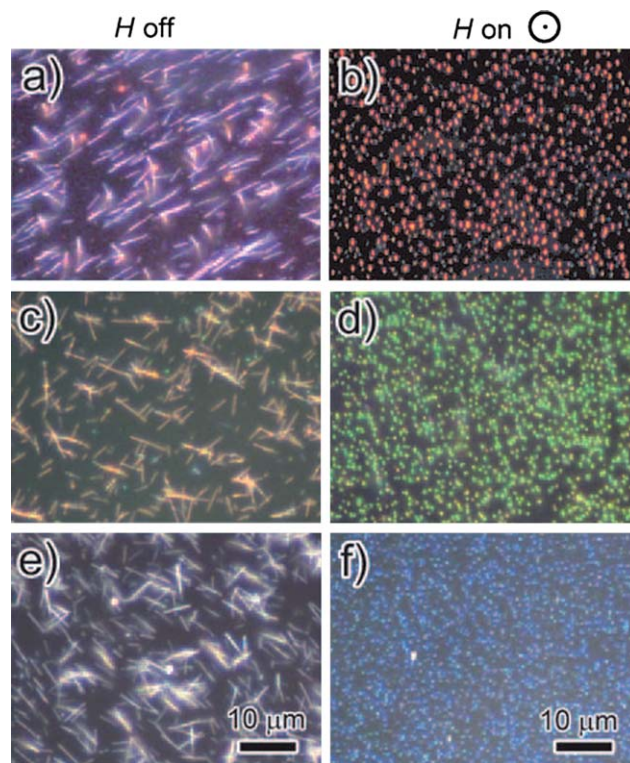
nanoshells with improved reproducibility for the synthesis and enhanced stability of the structure and optical properties. By tuning the pore structure of the silica networks through etching, one is able to control the shape/size of the Au NPs during the seeded growth, and consequently the interparticle plasmon coupling. The absorption peak of such multilayer structures can be effectively tuned from ∼520 to 900 nm of the near-IR region.

Fig. 8 shows the gradual change in the optical properties with the evolution of the nanoshell structure. The gallery of the as-obtained colloidal suspension displays a clear progression in color as the gold shell goes from dispersed seeds to completion. The original colloids, which contain a small amount of Au seeds, exhibit a light brown color which can be attributed to the absorbance of the Fe$_3$O$_4$ cores. When more Au is deposited onto the surface of the seeds, a reddish color appears due to the characteristic surface plasmon resonance of the colloidal Au particles. Upon further seed-mediated growth, the solution becomes dark red, then purple, and finally blue. This color change was also monitored by UV-vis absorption spectroscopy, as shown in Fig. 8(b). The original seed-containing colloids display two peaks at ∼420 and ∼518 nm, which can be attributed to the absorptions of Fe$_3$O$_4$ cores and gold seeds, respectively.[178] When the Au seeds become larger, the corresponding plasmon peaks red-shift from ∼518 to over 900 nm. The exact location of the plasmon peak can be tailored within this spectrum range by
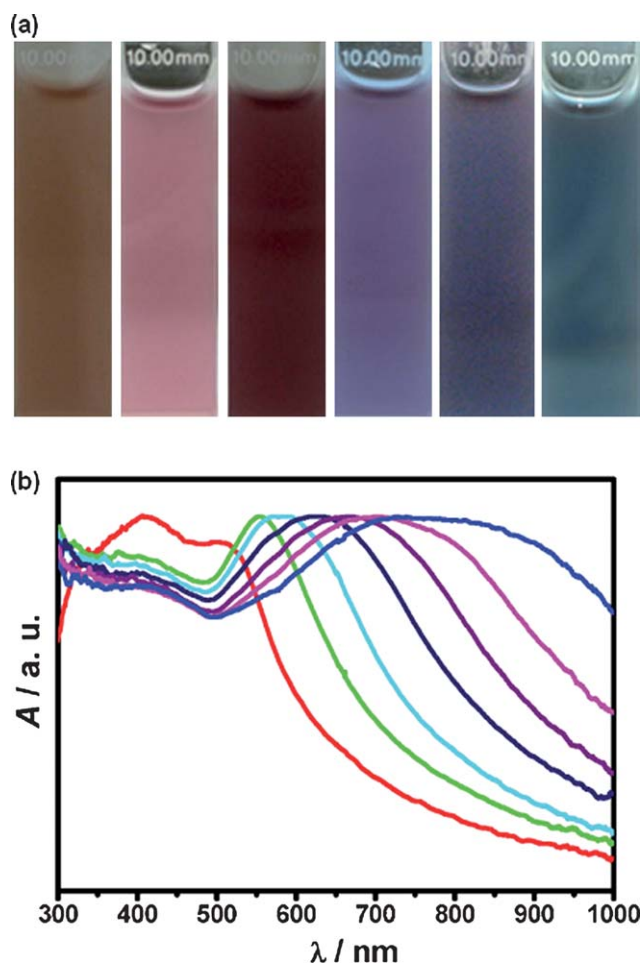
Fig. 8 (a) Digital photos showing the color of the nanoshell solutions after 0, 6, 8, 10, 12, and 16 cycles of seeded growth (from left to right). (b) UV–vis spectra presenting the evolution of optical property of the Au nanoshells after 0, 6, 8, 10, 12, 16, and 18 cycles of seeded growth (from left to right). (Reprinted with permission from John Wiley and Sons.)[177]

controlling the number of seeded growth cycles in a highly reproducible manner.[177]

This optical property has led to many important analytical and biomedical applications, for example, nanoshells can serve as active components in drug delivery, photothermal therapy, and surface-enhanced Raman scattering (SERS).[179–181] For applications in photothermal therapy, the nanoshells can be designed to strongly absorb near-IR light, which can penetrate soft tissue, by controlling the relative dimensions of the core radius and shell thickness so that the radiation energy can be effectively converted into thermal energy to kill nearby malignant cells.[177]

3.2 Magnetic properties

Magnetic NPs have potential applications such as magnetic data storage,[56,105,106,130] biomedical drug release,[57] microwave absorption[182–184] and environmental remediation.[107,185–187] The magnetic property is strongly dependent on the interparticle and intraparticle interaction, which can be controlled by the core size and the shell thickness. A SQUID magnetometer is normally used as a tool to test the magnetic properties of the nanomaterials. Temperature dependent magnetization investigations

reveal the blocking temperature (T_b) of the system and the magnetic moment of the magnetic atoms. Field dependent magnetization provides information on the intrinsic magnetic property (soft or hard materials differentiate from the range of coercivity, H_c) of the nanomaterials. Another important application of the SQUID magnetometer is to determine whether the iron-group metal core is oxidized or not. The detailed measuring procedure is to cool the samples at a higher magnetic field such as 1–5 tesla followed by recording the magnetization changes with changing the applied magnetic field. Then by comparing the hysteresis loop with the zero field cooled hysteresis loop, the iron-group metal core is oxidized if there is a shift toward the applied magnetic field. The principle for this technique is based on the exchange-coupling interaction between the ferromagnetic core and the antiferromagnetic shell.[158,188–190] More detailed information on how to apply this approach to investigate the chemical stability of the magnetic core is provided in the following section.

The shell materials have a dramatic effect on the magnetic properties of the magnetic core, which also strongly depend on the iron-group metal core size, materials, and crystalline structures. In addition, the shell structure, such as the shell thickness and crystallinity, has a significant impact on the core–shell NPs. Here, the effect of the shell material on the magnetic properties can be appreciated in the yttria-coated FeCo magnetic NPs and the alumina coated FeCo NPs.[64,65] The dramatic change is in the H_c. The yttria coated FeCo has a H_c of 1380 Oe[65] rather than the 1160 Oe for the alumina coated FeCo NPs.[64] The porosity inside the nanoparticle from the heat treatment and the shape anisotropy contribute to the magnetic property difference.[65]

The shell thickness also has an effect on the magnetic properties of the core–shell NPs.[128] However, the Fe–Au core–shell NPs fabricated by the sequential reverse micelle method with shell thicknesses of 2, 2.5 and 3 nm did not show any difference in T_b and H_c.[128] The fabricated Fe–Au core–shell NPs were stable under the magnetic measurement and powder diffraction, while the recent X-ray absorption spectroscopy (XAS) study showed the unstable property of the Fe–Au core–shell NPs.[123] Unlike the formation of the Fe–Mg core–shell NPs, the failure to fabricate core–shell NPs by annealing the Fe–Ag metastable alloyed NPs also indicates the instability of the core–shell structured Fe–Ag system. This unstable structure is also observed in the Fe–Au nanoparticle system. While the Co–Cu core–shell nanoparticle system has no unstable property, the very thin shell has a strong effect on the magnetic property such as enhanced T_b.[134] Comparing the shell effect on the Fe–Au and Co–Cu core–shell NPs, the authors here believe that there is a critical shell thickness from which the shell has a different effect on the magnetic properties. The interparticle coupling and intraparticle interaction are reported to have a strong effect on the magnetic property of the tiny NPs.[128] From this viewpoint, it is reasonable to deduce that the reported Cu shell is within the critical size range, where the intraparticle interaction has an important effect on the magnetic property. However, all the three Au shells are larger or equal to 2 nm; the intraparticle interaction is much weaker as compared with the interparticle interaction, which is also reported in the Fe–Au core–shell NPs.

The importance of the interparticle distance (spacing) in the magnetic properties is also reflected in the C–Fe[105] and polymer–Fe systems.[55,56,191,192] For example, a huge difference is observed

in the Fe–polyurethane (PU) polymer nanocomposites (PNCs), in which the particle loading and particle distance upon annealing under reducing environments play a role in the magnetic properties. Fig. 9 shows the room-temperature hysteresis loops of the as-received NPs and the PU PNCs. The saturation magnetization (M_s, 97.6 emu g^{-1}, based on the total mass) of the as-received NPs is lower than that of the pure bulk Fe (218 emu g^{-1})[193] due to the presence of oxide shells. The lower H_c (5 Oe) indicates a superparamagnetic behavior of the as-received NPs. Little difference in M_s is observed for the NPs after they are dispersed in the polymer matrix. The M_s of the PNCs, 54.0 and 31.6 emu g^{-1}, for the particle loading of 65 and 35 wt%, respectively, correspond to 84.0 and 90.2 emu g^{-1} for the NPs. The slightly lower M_s in the PNCs than that in the as-received NPs is attributed to the further oxidation of the NPs during the PNC fabrication process and the particle–polymer surface interaction effect.[194] The H_c values of the PU PNCs are 685 and 900 Oe for 65 and 35 wt% loadings, respectively, which are much larger than that of the as-received NP assembly. This behavior, however, is typical of magnetic PNCs.

The heat treatment at 250 °C does not show any significant changes in mass, volume, M_s, or H_c, indicating good thermal stability of the PNCs. However, the heat treatment at 450 °C brings about many changes. First of all, it carbonizes the matrix and reduces the oxide shells. The mass loss and shrinkage in the matrix effectively increase the particle loading for the PNCs. All these changes effectively increase M_s while reducing H_c. In the 65 wt% PNCs, H_c remains practically the same after heat treatment at 250 °C but decreases to 165 Oe after the additional heat treatment at 450 °C. This trend is due to the interparticle dipolar interaction within the PNCs with a good dispersion of single-domain NPs, consistent with particle-loading-dependent coercivity in nanoparticle assembly.[195] Compared with the 35 wt% PNCs, the smaller H_c in the 65 wt% PNCs arises from the decreased interparticle distance concomitant with a stronger

dipolar interaction. The further decrease in H_c after the 450 °C heat treatment is for the same reason, i.e., the decreased inter-particle distance resulting from shrinkage. In addition, the presence of an oxide shell around the metallic core is reported to increase T_b of NPs through the exchange coupling interaction between the ferromagnetic metal core and the antiferromagnetic oxide shell.[156] Thus, the loss of the exchange coupling in the heat treated PNCs due to the disappearance of the antiferromagnetic oxide shell also contributes to the smaller H_c. HRTEM observation revealed an iron core coated with carbon shell structure.[105]

Due to the unusual multiphase polycrystalline structure of the NPs favoring the noncollinear arrangement of the magnetic moments and to the highly disordered magnetic surface layers from the high specific surface area, the core–shell NPs have anomalous magnetic behaviors. The positive or negative effect also depends on the core–shell materials. In the Ag coated Co NPs, H_c and remanence (also called remnant magnetization, M_r) at room temperature are weak and no magnetization is saturated even at a field of 1 tesla.[136]

Furthermore, clusters of a Co core with a noble metal shell have been studied with theoretical calculation using a parameterized tight-binding model[196] and a spin-polarized s–p–d tight-binding model[197] and it has been predicted that the noble metal (Cu) develops a net polarization that changed the total magnetic moment of the clusters. It was predicted that the size, shape and materials of the shells have an effect on the magnetic properties.[196] Thus, the magnetic properties of the Co NPs are expected to differ from those of Co NPs with a noble Au or Cu shell.

Another important effect of the reactive shell such as Mg is that it can prevent the oxidation of the metallic magnetic core by the formation of a thin layer of MgO,[144] which retained the magnetic property of the core even after long term exposure to air.

3.3 Oxidative stability

The stability of the iron-group metal core is a very important factor for the application of core–shell NPs, which are normally operated in an ambient condition or acidic environments. The carbon coated iron-group metal NPs synthesized by the modified arc discharge method are found to be very stable for months even in the strong acids such as aqua regia (a 3 : 1 mixture of HCl and HNO$_3$)[104] and the C–Fe core–shell NPs synthesized by heat treatment of PNCs under a reducing agent also show great stability in acids.[105,107,198,199]

The simplest way to test the core stability is to expose the core–shell NPs in acids. The core is oxidized into ions and dissolved in the solution, which will bring about the loss of the magnetic property and is not found in the carbon coated ferromagnetic metal core[104] and Cu coated Co NPs.[134,200] The easy way to prove a complete shell is to use the HRTEM. TEM is an effective way to see the micrograph (shape and the size) of the particles or even the core–shell interface if the atomic number difference is large. Even more, a powerful ability of TEM is to see the lattice fringes that are characteristic patterns of the specific atoms. With a large atomic number difference between core and shell elements such as in carbon–nickel shell–core NPs, the core–shell interface can be easily distinguished by the lattice distance in the lattice fringes, Fig. 10, for the graphite coated Ni NPs.[104,201] The contrast
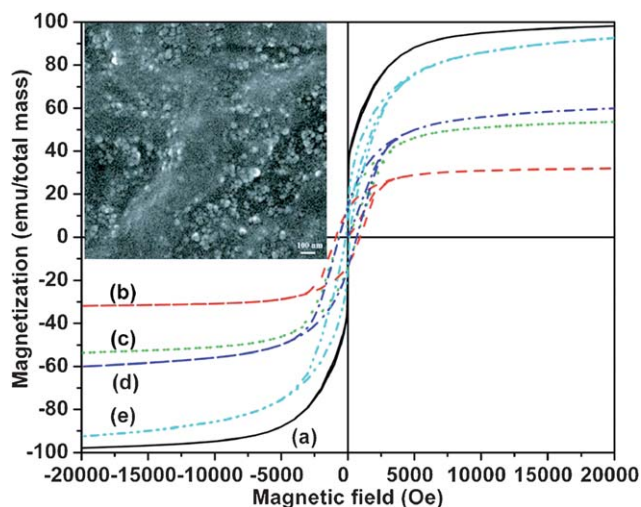

Fig. 9 Hysteresis loops of (a) as-received NPs; nanocomposites with a particle loading of (b) 35 wt% and (c) 65 wt%; and nanocomposite with 65 wt% particle loading with heat treatment at (d) 250 °C for 2 h and (e) 450 °C for additional 2 h. The inset shows the SEM image of the nanocomposite with a 65 wt% particle loading. (Reprinted with permission from American Institute of Physics.)[105]
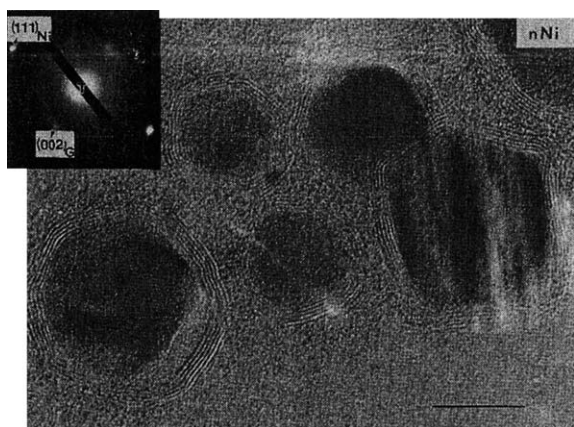
Fig. 10 HRTEM micrograph of graphite-coated nickel NPs. (Inset, nanodiffraction pattern for graphite (002) and nickel (111) reflections. Scale bar, 10 nm.)[104]

difference with respect to the electron beam has been reported as a distinguishing criterion for a core–shell structure.[40,160,202,203] The typical core–shell NPs as observed in TEM are shown in Fig. 11 for the PS–Fe_2O_3 core–shell NPs.[160] It is difficult to distinguish between the core and the shell if the lattice constants are almost the same and the atomic numbers are similar such as in the Co–Cu core–shell NPs.[134] The limitation here is that the atomic number should have enough difference between the targeting core and shell metals. In addition, XRD is normally used to determine the structure of NPs and can determine the component constitution and phase structure of the product, from which the alloyed or core–shell structure can be derived under the condition that the nanomaterials are big enough.

Another normally adopted method for the discrimination of core stability is to monitor the magnetic behaviors under the zero field cooled (ZFC) and field cooled (FC) hysteresis loop. The principle here is that the existence of the antiferromagnetic layer around the ferromagnetic core will lead to the exchange-coupling interaction i.e. the shift of the hysteresis loop toward the magnetic field.[158,188–190] The surface of the metallic NPs was oxidized if there was a hysteresis loop shift toward the applied
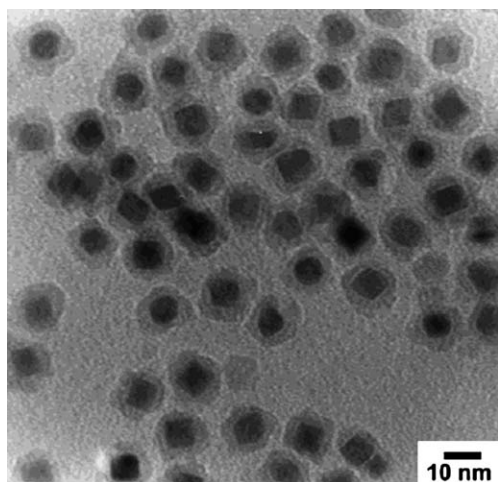

Fig. 11 TEM image of the PS–Fe_2O_3 core–shell NPs. (Reprinted with permission from American Chemical Society.)[160]
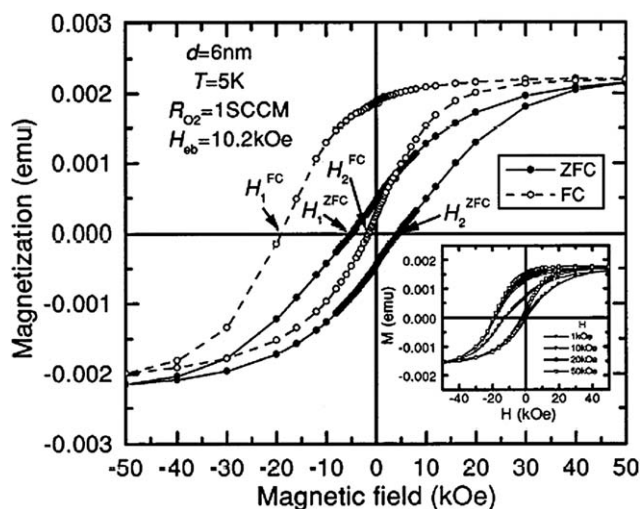

Fig. 12 Hysteresis loops of ZFC and FC Co/CoO NPs with a size of 6 nm prepared at the oxygen gas flow rate of 1 SCCM. (Inset: FC hysteresis loops in different magnetic fields.)[188]

magnetic field. The scheme of the shift is shown in Fig. 12. Fig. 12 shows the ZFC and FC hysteresis loops for the Co–CoO NPs with a particle size of around 6 nm and a shell of around 1 nm. The large shift was observed, indicating the existence of cobalt oxide. In addition, the inset of Fig. 12 shows the FC hysteresis loop at different applied cooling magnetic fields. It was noticed that the shift increased with increasing the cooling field and almost was stable when the cooling fields are higher than 1 tesla.[188]

In addition to the shift of the FC hysteresis loop toward the magnetic field as compared with the ZFC hysteresis loop, the ZFC hysteresis loop also exhibits a two step saturation behavior. The scheme is shown in Fig. 13. Fig. 13 shows the hysteresis loops of the 9 nm Fe core NPs with a shell thickness of 2–3 nm iron oxide, and pure Fe_3O_4 NPs with a size of 10–15 nm at 5 K. For the iron oxide coated Fe NPs, the hysteresis loop shows a two-step saturation behavior with the rapidly saturated part corresponding to ferromagnetic Fe cores and the slowly saturated part to the ferromagnetic iron oxide shell with a thickness of 2–3 nm. For the pure iron oxide NPs, there is no sharp change in the hysteresis loop (Fig. 13(b)) when compared with Fig. 13(a) for the iron oxide coated Fe NPs. The inset shows the hysteresis loops of the iron oxide coated Fe and pure iron oxide NPs at different temperatures. The magnetization does not saturate even at 5 tesla, which is due to the surface spin disorder state of the ferromagnetic iron oxide nanoparticle system.[204] This phenomenon can be used as a tool for the discrimination of the surface oxidation of the metallic core NPs.

XRD measurement is an effective way to determine the material components and the structures. The limitation, here, is that the gold peaks display large Scherrer broadening, which will hinder the diffraction from the Fe component of the sample, making it impossible to provide the iron state in the iron samples.[123] X-Ray absorption near edge structure (XANES) is very sensitive to the electronic structure (i.e. oxidation state and effective charge) of the absorbing atom, coordination geometries and different bonding types.[205–210] By comparing the measured
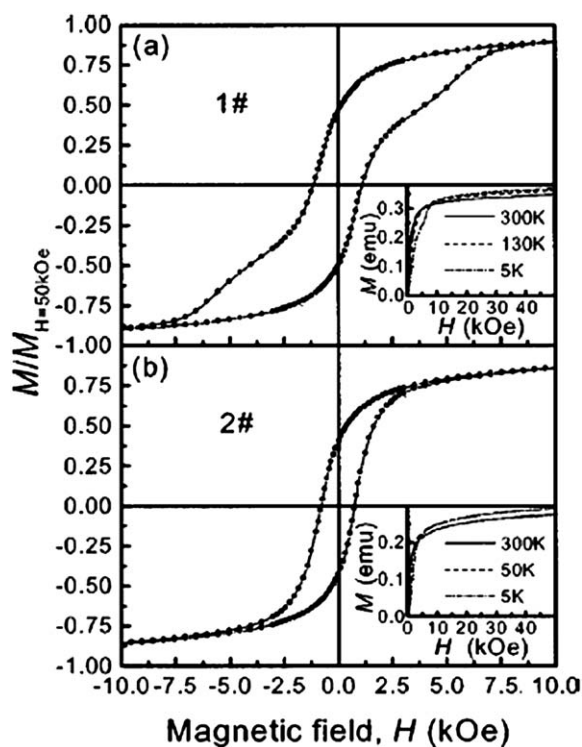
Fig. 13 Hysteresis loops of the (a) 9 nm Fe core NPs with a shell of 2–3 nm iron oxides and (b) Fe_3O_4 NPs with a size of 10–15 nm at 5 K. (The inset shows the initial magnetization curves at different temperatures.) (Reprinted with permission from American Institute of Physics.)[204]

Fig. 14 XANES spectrum of a Au/Fe/Au, Fe/Au NPs, standard bcc Fe metal, and $\gamma\text{-}Fe_2O_3$. (Reprinted with permission from American Institute of Physics.)[123]

Fig. 15 Co K-edge XANES spectra of a standard hcp Co foil, Co NPs, Co–Cu NPs, Co NPs oxidized in air, and CoO and Co_2O_3 references. Lines A, B, C, and D are the zero valence Co pre-edge, Co white line, and CoO and Co_2O_3 white lines, respectively.[134] (Reproduced with the permission of The Electrochemical Society).

spectra of the substance under investigation to the spectra of the well characterized standard reference samples, known as XANES fingerprinting, information on the above electronic and geometric properties such as valence state of the materials can be provided. The application of X-ray absorption spectroscopy (XAS) to the core–shell systems allows for the element-specific analysis of both the core and the shell. This method has been used in the Fe–Au[123] and the Co–Cu[134] core–shell NPs and will be discussed in the following.

Fig. 14 shows XANES spectra of Au/Fe/Au NPs, Fe/Au NPs, and two standard compounds—bulk bcc metallic Fe foil and bulk $\gamma\text{-}Fe_2O_3$. The XANES spectra of the NPs are quite different from that of the Fe foil and very similar to that of iron oxide.[123] This indicates that the reverse micelle noble metal shell coating has some disadvantage in protecting the iron core from oxidation even during the shell formation process or even before the shell formation.

This XAS technique was also demonstrated in the Co–Cu core–shell NPs. Fig. 15 shows Co K-edge XANES spectra of a standard hcp Co foil, Co NPs prepared in a glove box with nitrogen protection, Co–Cu NPs exposed to air, Co NPs exposed to air and two standard cobalt oxides. The XANES spectrum of the cobalt in the Co–Cu core–shell NPs differs from the cobalt oxide spectra and is very similar to the standard cobalt foil and the Co NPs under nitrogen protection. The cobalt K-edge XANES spectrum of the Co–Cu nanoparticle sample exhibits a pre-edge feature at approximately 7709 eV (line A), assigned to an electron transition from 1s to a hybridized p–d orbital, and a white line at about 7724 eV (line B). The position of the
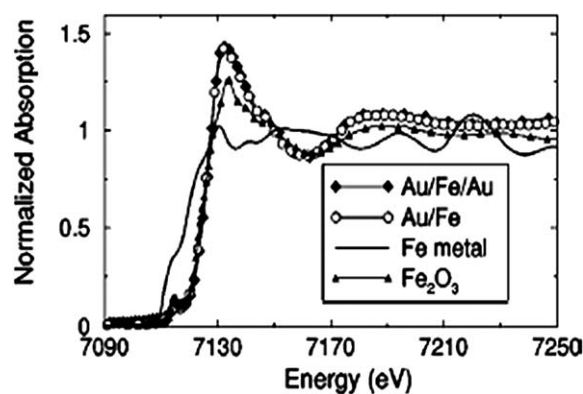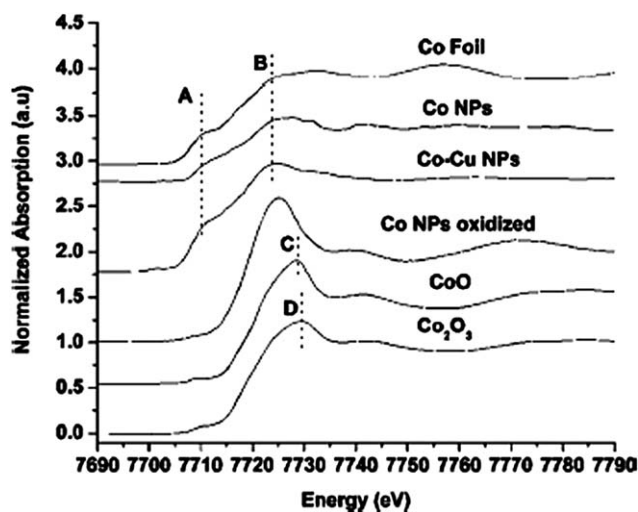
absorption edge in the Co–Cu spectrum, as well as the intensity, and the energy location of the maximum white line closely resemble those of the Co NPs protected under nitrogen and the standard hcp Co foil. The shift toward higher energy for the two standard cobalt oxides and the Co NPs exposed to air was not observed for the Co–Cu NPs and the Co NPs protected with nitrogen. This indicates that the acidic electrolyte synthesized Cu shell around the Co core NPs has successfully protected the Co core from oxidation.

3.4 Surface functionality of the shells

Fabrication of a shell around iron-group NPs provides a unique opportunity for the attachment of organic molecules and biological molecules onto the surface of the shell. Gold coating can be easily functionalized with various organic species such as through the strong Au–S bond. The polymer shell can also be

easily functionalized with organic molecules for further applications.

4. Applications of core–shell nanoparticles

It is well known that the NPs especially iron-group metals are very reactive and can be easily oxidized in ambient conditions, which limits their potential applications such as the magnetic data storage. The introduction of the noble metal shell enhances the applications of iron-group NPs in the harsh environments such as acidic or basic solutions.

However, the easy oxidation of the iron-group metal NPs is not always bad for some reasons such as an improved blocking temperature.[156] Compared with Pd, Au, and Pt, the iron-group metals are cheap and more reactive. It is much more economical to obtain the nanoshell around the Fe and Ni cores instead of the solid Pd and Pt NPs, in which the core is a waste of the material in the catalyst applications. The more reactive iron-group NPs can serve as the substrate for the subsequent shell formation and serve as a reducing agent to reduce the shell metal ions. The introduced noble metal shell can also enable the core NPs to survive in the aqueous solution, which is the normal condition for the biological applications. The following potential applications such as catalysis, magnetoresistance sensor, biological drug delivery, and environmental remediation will be discussed with detailed examples.

4.1 Catalytic application

The core–shell structures have been widely used as catalysts, and the functions of the core or the shell vary among different reactions. Generally, the core–shell catalysts can be divided into three groups: (1) the core serves as the support and the shell is the active site, (2) the core is the active site and the shell works as the protector, and (3) both core and shell are active sites. In the following parts, we will provide a brief review on the catalytic applications of core–shell structures.

Pd and Pt NPs have been used as catalysts for many reactions.[211–219] The active parts of the catalysts are the surface of the NPs and the large part of the expensive metal in the core is a waste. Introducing the cheaper metals as the core such as Ni and Cu is an effective way to economize the catalyst production cost. Furthermore, the introduction of the cheaper core such as Ni within the Pd shell NPs was reported to enhance the catalytic efficiency in the Sonogashira coupling reaction.[132] The Ni–Pd core–shell NPs (3.9 nm) show a much better catalytic effect than the pure Pd NPs (3.5 nm) with a comparable particle size, Fig. 16. The enhanced catalytic activity is due to the large number of Pd atoms on the particle surface as compared with the same amount of pure Pd NPs.[132]

The Ni–Pd core–shell NPs have also demonstrated a similar catalytic effect on the CO oxidation as the pure Pd NPs, but totally different from that of the pure Ni NPs, Fig. 17. Pure Ni NPs are active only at higher temperatures. The deactivation was not observed in the Ni–Pd core shell NPs indicating that the core–shell structure is stable and does not form an alloyed structure during the catalytic reaction process. The very close CO oxidation behavior between the core–shell NPs and the pure Pd NPs provides the advantage of the core–shell structural NPs to
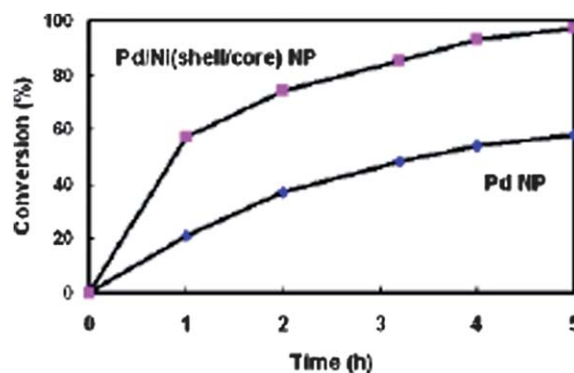

Fig. 16 Catalytic activity comparison between Ni–Pd core–shell NPs and pure Pd NPs. (Reprinted with permission from American Chemical Society.)[132]

save the more costly Pd core for the catalysts.[133] The supported Ni catalysts such as Ni/Al_2O_3, $Ni/MgO–Al_2O_3$ with a core–shell structure have also been proven to be promising in all types of methane reforming reactions, such as partial oxidation of methane, steam reforming, and CO_2 reforming (Fig. 17).[220]

In many catalytic reactions, although the metal NPs were reported to be active, their long-term stability either in solutions or at high temperature conditions is always a critical problem. Especially when the reaction temperature is high, tiny NPs start to melt and agglomerate together, yielding larger particles. One strategy is to design the core–shell-type nanocatalysts that have active catalyst nanoparticle cores protected by porous silica shells.[221] The silica shells behaved as a blocking layer that isolated each nanoparticle from the neighboring ones but penetrated the molecular reagents through their mesopores. Park et al.[222] synthesized $Ni@SiO_2$ yolk–shell nanocatalysts that bear tiny Ni cores with an average diameter of 3 nm. The Ni NPs were coated with silica through the microemulsion method and the
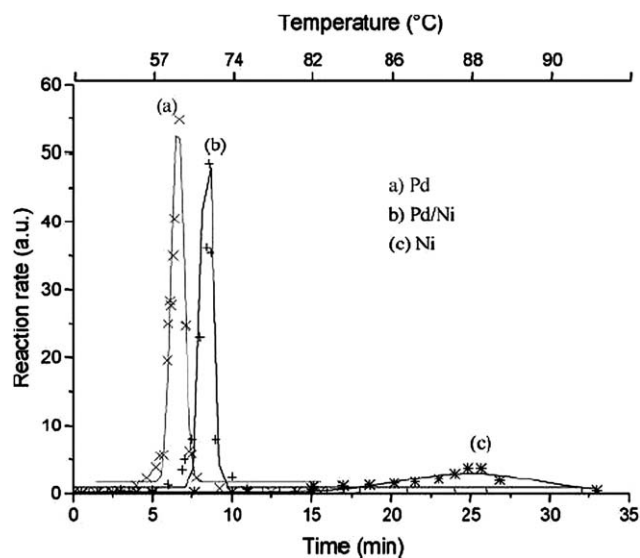

Fig. 17 CO_2 production rate in the reactor as a function of the time, during heating from room temperature to 100 °C for the pure Pd, Ni–Pd core–shell, and pure Ni NPs. (Reprinted with permission from American Chemical Society.)[133]
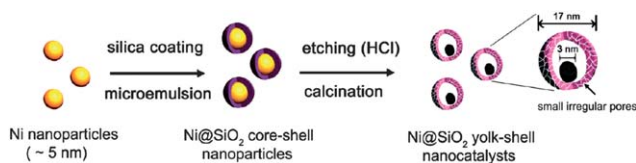
Fig. 18 Synthesis of Ni@SiO$_2$ yolk–shell nanocatalysts with tiny nickel cores. (Reprinted with permission from American Chemical Society.)[222]

resulting Ni@SiO$_2$ core–shell NPs were partially etched by acid treatment. The calcination of the particles yielded yolk–shell nanocatalysts with a uniform structure, Fig. 18. The catalysts were proven to be very active and highly stable for hydrogen-transfer reactions of acetophenone; no significant activity loss was observed after six cycles. These Ni@SiO$_2$ core–shell NPs have also been employed as a model catalyst for the steam methane reforming reaction. The catalysts exhibit a continuous conversion rate of methane and hydrogen, and significantly enhanced stability at high temperatures, leading to a high recyclability without loss of catalytic activity.[223] This rational core–shell design of the nanocatalysts has also been employed for other important reactions with the advantages of high reactivity and reusability, for instance, Au@SiO$_2$ for *p*-nitrophenol reduction,[222] Au@ZrO$_2$ for CO oxidation,[224,225] and α-Fe$_2$O$_3$@SiO$_2$ for ammonia decomposition.[226]

Although encapsulation within porous shells makes the metal NPs catalytically active and at the same time keeps them stable even under harsh reaction conditions, the recyclability is another concern for practical applications.[227–229] Ge *et al.*[230] designed a novel core–satellite nanocomposite catalyst, Fig. 19. A monolayer of the metal nanocatalyst is first immobilized on the surface of silica colloids by using coupling agents. The core–satellite structures are then coated with another layer of silica with a desired thickness to fix the position of metal NPs. Finally,
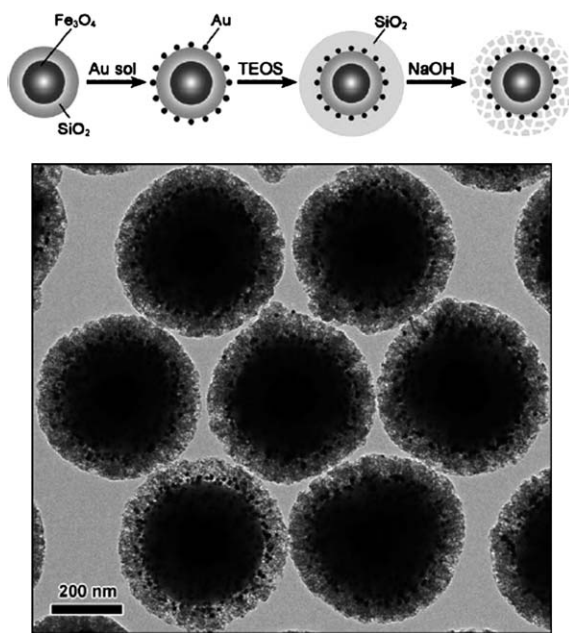

Fig. 19 Synthetic procedure and a typical TEM image of porous silica protected Fe$_3$O$_4$/SiO$_2$/Au composite structures. (Reprinted with permission from John Wiley and Sons.)[230]

a "surface-protected etching" technique is applied to make the outer shell mesoporous, which makes the catalyst particles exposed to the outside chemical species. To improve the recyclability, a super-paramagnetic Fe$_3$O$_4$ core was incorporated at the center of the initial silica colloids. Liquid-phase reduction of 4-nitrophenol (4-NP) by NaBH$_4$ was used as a model reaction to characterize the performance of the Au catalyst system. Both the rate constant and the turnover frequency (TOF) suggested higher catalytic efficiencies for Au nanocatalysts confined in the shells with larger mesopores. The enhanced diffusion of reactants through the larger pores is believed to be responsible for the increased catalytic efficiency. The magnetic moment of the Fe$_3$O$_4$ core in the composite structures is sufficiently high that a complete separation of the catalyst colloids from the reaction solution can be achieved within 1–3 min in a relatively low magnetic field gradient (<30 T m^{-1}).[230]

In terms of the consecutive reaction (A → B → C), an active catalyst generally contains two types of active sites, one of which accelerates the reaction of A to B and the other accelerates the reaction of B to C. Improving the dispersion of these two kinds of active sites, whilst ensuring they are still close to each other, is the most efficient approach to enhance the catalytic performance.[231] However, the easy migration of the first reaction products to the active sites of the second reaction determines the selectivity of the final products. For the conventional bifunctional catalysts, different active sites are randomly distributed on their surface, providing an unrestricted, open reaction environment where the coupled reactions occur independently and randomly, even though the distance between the two active sites is very short. This means that the products desorbed from the first reaction sites can leave the catalyst without reacting further at the other active sites.

To enhance the easy migration of the reactants to the active sites and to improve the selectivity of this consecutive reaction, Bao *et al.*[232] designed a novel bifunctional catalyst with a core/shell structure where the core and shell components independently catalyze different reactions. The shell consists of a membrane layer containing a pore path. The reactants must first pass through the shell membrane to reach the inner core catalyst, where they react to form the intermediate products. To leave the catalyst, all the intermediates must enter the membrane channels, where they have a very good chance of being converted into the final products at the active sites in the membrane. With this design, Bao *et al.*[232] coated an H-beta zeolite membrane onto the surface of Co/Al$_2$O$_3$ catalyst pellets to form a core/shell structure, Fig. 20. The prepared catalyst showed an excellent performance for the direct synthesis of isoparaffins based on the Fischer–Tropsch synthesis (FTS) reaction. The formation of C$_{12+}$ hydrocarbons is suppressed completely and the middle isoparaffins become the main products. A desirable low selectivity for methane is also achieved. This core/shell membrane catalyst provides a tailor-made confined reaction environment, which results in spatially confined effects and shape selectivity. This great idea was further extended to other consecutive reactions as the shell and core components are independent catalysts of different reactions. For instance, a novel double-shell catalyst with silicalite-1 zeolite and H-ZSM-5 zeolite coated on a bimetallic Cr/ZnO core was developed by Yang *et al.*[233] for the one-step, well-controlled synthesis of dimethyl ether from CO$_2$ containing syngas.
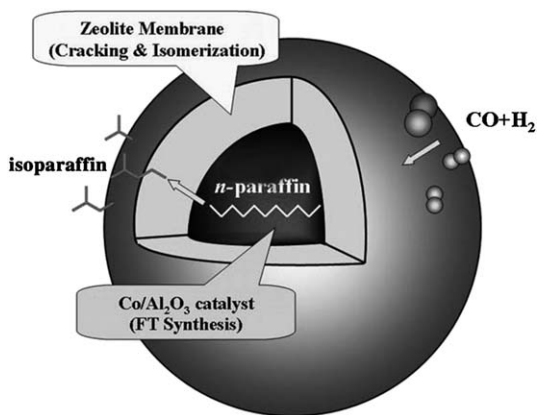
Fig. 20 Representation of the core/shell catalysts for consecutive reactions. (Reprinted with permission from John Wiley and Sons.)[232]

The core–shell structures have also been employed in the photo-catalysis. Previous studies have shown that the metal NPs deposited on the TiO_2 nanostructures undergo Fermi level equilibration following the UV-excitation and enhance the efficiency of the charge-transfer process.[234,235] In most of the catalytic studies, metal NPs are dispersed on an oxide surface. Such a catalyst structure effectively results in exposing both metals to reactants and the surrounding medium. Corrosion or dissolution of the noble metal particles during the operation of a photo-catalytic reaction is likely to limit the use of noble metals such as Ag and Au.[236,237] To overcome these drawbacks, Hirakawa and Kamat[238] prepared $Ag@TiO_2$ core–shell clusters by a one pot synthesis method that involved reduction of metal ions and hydrolysis of titanium-(triethanolaminato) isopropoxide in dimethylformamide (DMF). The synthesis process is shown in Fig. 21. The result indicated that the photo-excitation of the TiO_2 shell results in an accumulation of the electrons in Ag, and the stored electrons can be discharged when an electron acceptor such as O_2, thionine, or C60 is introduced into the system. The charge equilibration between the metal and semiconductor plays an important role in dictating the overall energetics of the composites. These metal core–semiconductor shell composite
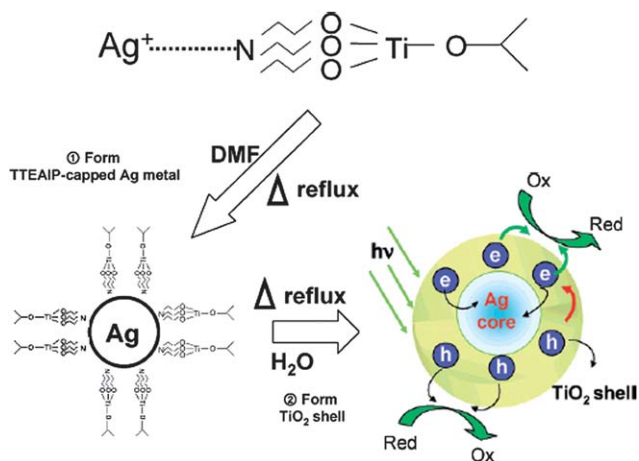

Fig. 21 Preparation procedure of the $Ag@TiO_2$ core–shell photo-catalysts. (Reprinted with permission from American Chemical Society.)[238]

clusters are photo-catalytically active and are useful to promote light induced electron-transfer reactions. Their results also suggested the design of semiconductor–metal composite nano-structures for light energy harvesting applications.

4.2 Giant magnetoresistance (GMR) sensing

The Nobel Prize in Physics was awarded to Drs Fert and Grunberg in 2007 for their work on the giant magnetoresistance (GMR, a resistance change with the applied magnetic field) discovered in 1988,[239–241] which has revolutionized the information industry[242–245] with an increased recording density of the hard disks. GMR sensors provide a convenient way of sensing the relative motion and position of objects without physical contact (non-contact/non-destructive).[246,247] Just attach a magnet to one object and a GMR sensor to another. Alternatively, if one of the objects contains a magnetic material such as iron or steel, the object in motion will alter any magnetic field, which can be detected by a GMR sensor.[248] GMR applications of this motion/position effect could become widespread in the industrial, transportation, aerospace, and military worlds.[249–251]

GMR, discovered in a multilayered Co/Cr system in 1988, is a result of the spin dependent conductivity of electrons especially in a conductive material composed of alternative ferromagnetic and nonmagnetic layers.[252] Under zero external magnetic field, the magnetization directions of the adjacent ferromagnetic layers in a GMR material are anti-parallel due to an anti-ferromagnetic coupling between the layers. Thus, electrons with spin up as well as spin down are scattered by the alternating magnetic fields, resulting in a high electrical resistance. When an applied field aligns the magnetization in these adjacent ferromagnetic layers, electrons with their spins parallel to the magnetization can travel with less scattering and hence a lower level of resistance is observed. The electrical resistivity drops when the applied magnetic field overcomes the antiferromagnetic coupling and the magnetization orientation becomes parallel. Fig. 22 shows the electron transport in the multilayer GMR material under zero field and applied field conditions, respectively.

Similar to multilayer materials, a granular structure with nanoscale ferromagnetic grains separated by a non-magnetic conductive matrix can show the GMR effect, Fig. 23. The first reported granular GMR effect was in Cu/Co composites where Co granules were embedded in a Cu matrix.[253] Since then, a number of other metal matrix composites have been found to have the GMR effects.[254] However, the signal is lower than 1% even at lower temperatures such as 5 K and the easy oxidation of the metal grains put a limitation for certain applications.

A standard four-probe technique to minimize the contact resistance is normally used to measure the resistance change with
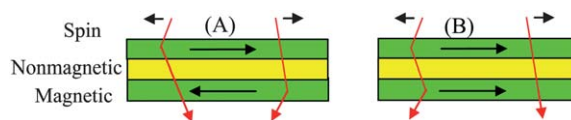

Fig. 22 Schematic of the electron transport in a multilayer GMR material under different magnetic domain orientations: (A) anti-parallel under no applied magnetic field and (B) parallel under an applied magnetic field.
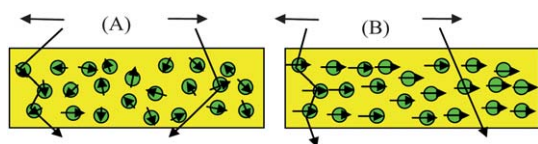
Fig. 23 Schematic of a granular GMR material: (A) no and (B) applied magnetic field.

the applied magnetic field. It was reported[255] that the GMR effect would disappear if the nonmagnetic layers were thicker than the electron mean-free path and consistent with the theoretical prediction by the RKKY theory (an abbreviation derived from the names: Ruderman, Kittel, Kasuya and Yosida).[256] The mean free path describes the average distance, in which the conduction electrons are accelerated. For metals, it is in the order of 10 nm.[255] Thus, the exchange coupling will decrease with an increase in the nonferromagnetic layer thickness.

Granular materials, consisting of a discrete magnetic phase in a non-magnetic material matrix, exhibit GMR. Compared to the multilayer GMR sensor, the granular structure has many advantages: simple and low-cost preparation[256–258] and easy particle size control by the different annealing temperatures.[259,260] The granular structure is usually prepared by co-deposition of magnetic and nonmagnetic metals. In codeposition nanoparticle preparation, the nonmagnetic and magnetic phases are immiscible. The formed NPs will be metastable and will form an egg-shape structure at higher temperature. Also co-deposition (sputtering) of the composite material target (metal source) will give a granular structure.[261] Another method for obtaining a granular structure is molecular beam epitaxy (MBE) for the Co/Cu and Co/Ag films.[262] The granular structure can be thought of as a special form of NPs. The resistance changes with the spin-dependent scattering. The discrete NPs will align parallel to each other in an applied external magnetic field. In this respect, both the multilayer and the granular structure have the same GMR origin.

The important factors governing the extent of GMR performance include: size of the discrete phase,[263] distance between the two magnetic layers (nonmagnetic layer thickness), composition of the granules,[264] and shape of the GMR materials which will lead to the shape anisotropy. The annealing temperature on the thin film will also have an effect on the GMR performance. It reduces the structural disorder but increases the segregated phase size and interparticle distance in alloys. The two different materials in magnetic and nonmagnetic layers need to be immiscible or they will lose the interface between the two phases by diffusion into each other.[255]

Here, the Fe–Au core–shell NPs were used as an illustrative example of the resistance change with the applied magnetic field. The used Fe–Au core–shell NPs were prepared by sequential reverse micelle method. The granular thin film was prepared by the cold press method with a pressure of 2×10^7 Pa for 10 minutes. Fig. 24 shows the temperature dependent resistance for the cold pressed pellet of Fe–Au core–shell NPs. The resistance increases slightly with the increase of temperature, Fig. 24(a), indicating the metallic conduction rather than the thermally activated behavior, characteristic of a negative temperature coefficient. The negative MR was observed with about −0.17% at
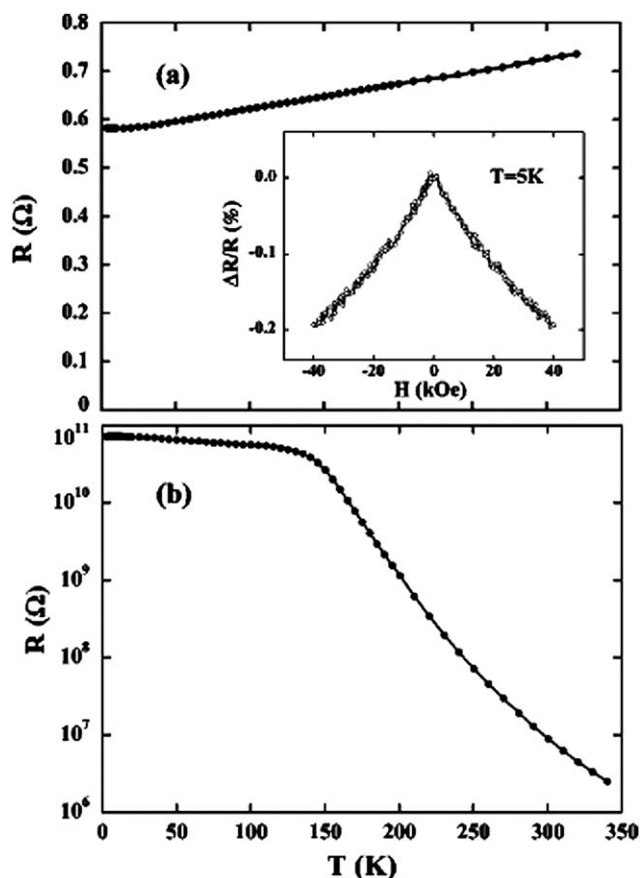

Fig. 24 Temperature dependent resistance of pressed Fe–Au nanoparticle pellets in zero magnetic field for (a) freshly prepared sample and (b) 1 month after synthesis (inset shows the corresponding magnetoresistance at 5 K).[265]

a field of 4 tesla, inset of Fig. 24(a). The resistance change with the magnetic field is caused by spin-dependent scattering.[265] In the Fe–Au nanoparticle pellet, the Fe cores serve as a magnetic scattering center. The magnetization orientation of each Fe core is random and results in a spin-disordered state under zero magnetic field condition. The Fe cores will align each other reducing the spin disorder, which in turn will reduce the spin-dependent scattering and subsequent resistance. The oxidation of the Fe–Au core–shell NPs was manifested in the electrical transport property. The resistance of the pellet after exposure to air for 1 month is much larger than that of the fresh sample. The negative temperature coefficient was also observed in the aged pellet sample, Fig. 24(b), indicating the thermally activated behavior at high temperature.[265] The increased resistance in the aged sample over the fresh sample indicates that the iron oxide has higher resistance as compared with Fe.

As a further illustration of the fact that MR can be achieved in the core–shell system, the iron–iron oxide core–shell NPs pellet was recently reported to possess negative MR.[266] Fig. 25 shows the field dependent MR of the Fe–iron oxide core–shell NPs with an averaged size of 8 nm and 18 nm, respectively, and the shell thickness of 2 nm. The observed MR depends on the measured temperature and also on the particle size. The positive and negative temperature coefficients for different sizes are shown in
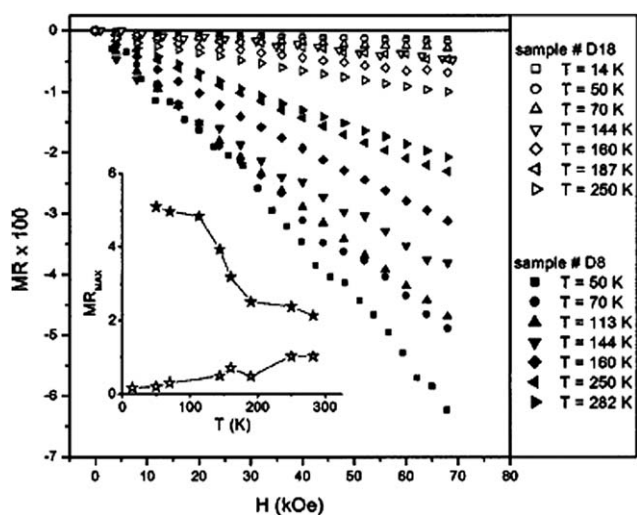
Fig. 25 Field dependent negative MR for the core–shell systems. Inset shows the temperature dependent MR. (D8 and D18 represent the 8 and 18 nm NP, respectively.)[266]

the inset of Fig. 25. This also indicates that the size or the ratio of the core–shell has an effect on the MR value and the transport mechanism.

Recently, Guo and co-workers have investigated the MR of carbon Fe nanocomposite systems. The GMR relationships with the temperature and particle loading have been reported. Fig. 26 shows the MR as a function of the field in the annealed polyacrylonitrile (PAN)–Fe PNCs fabricated by a novel solvent-extraction method.[56] The field required to saturate the MR is very high and is beyond the limit of the machine, which is a characteristic of the tunneling conduction mechanism. MR increases with the particle loading increasing from 10 to 20% and remains constant after the loading reaches 30%. The observed highest GMR is about 5.1% at room temperature. However, in the annealed vinyl ester resin (VER) PNCs filled with Fe NPs, a room temperature MR of 8.3% is observed in the heat-treated PNCs with an initial particle loading of 15 wt%, Fig. 27, whereas
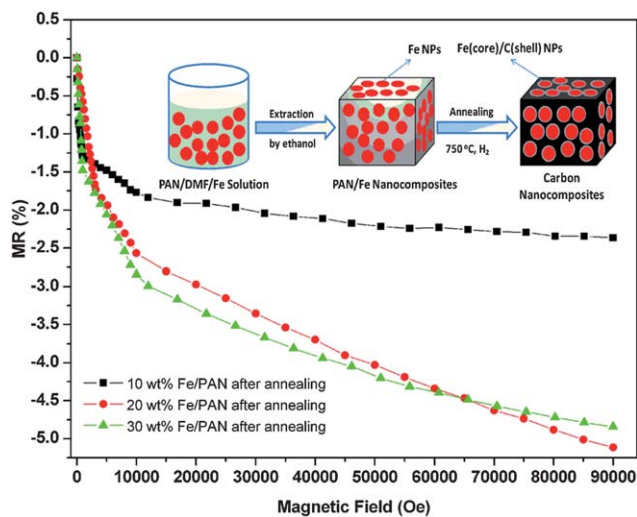

Fig. 26 Room temperature MR as a function of applied field for heat-treated PAN/Fe PNCs with an initial particle loading of 10, 20, and 30 wt%, respectively (inset shows the nanocomposite fabrication).[56]
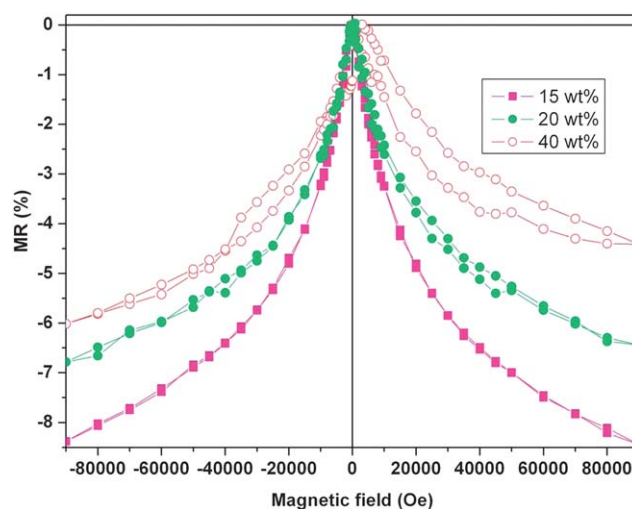

Fig. 27 Room temperature MR as a function of applied field for heat-treated VER PNCs reinforced with a Fe particle loading of 15, 20, and 40 wt%, respectively.[106]

the heat-treated PNCs with initial particle loadings of 20 and 40 wt% show a room temperature MR of 6.8% and 6.0%, respectively. All of these GMR values are observed at a fairly high field of 90 kOe. The particle-loading dependent MR is attributed to the interparticle distance. In addition, the spacer materials (VER and carbonized VER) play a role in the MR property. The observed field dependent MR hysteresis loops (Fig. 27) in the PNCs with high particle loadings are also due to the decreased interparticle distance together with a strong interparticle dipolar interaction. Similarly, a room-temperature MR of 7.3% is observed in the annealed Fe/PU PNCs.[105]

4.3 Microwave absorption

Due to their prospective applications in electronic instruments in industry, commerce, and military areas, the microwave absorbing materials have received great attention.[267] Most of the microwave absorbing materials are composed of magnetic loss powders such as ferrite,[268,269] nickel,[270] cobalt,[271,272] and dielectric loss materials such as carbon materials,[269] metal oxides,[273–276] and conducting polymers.[277]

Due to their excellent electrical conductivity, light weight, and low cost, magnetic particles encapsulated within CNT composites and magnetic particles coated by carbon have been the focus of extensive study.[269,278–283] For instance, Liu et al.[284] reported an absorbing medium of nanosize carbon black (CB) blended with nanosize silicon carbide (SiC). When 5 wt% carbon black is blended with 50 wt% SiC to fabricate a composite with a 2 mm thickness, the maximum reflection loss (RL) becomes −41 dB at 9 GHz and −10 dB when the bandwidth reaches 6 GHz. Che et al.[269,280] have reported that magnetic NPs/CNTs exhibited improved microwave absorption properties because of their proper EM matching between the dielectric loss and the magnetic loss. Fig. 28 shows two types of Fe encapsulated within CNTs. The absorption property is shown to result from the confinement of crystalline Fe in carbon nanoshells and derives mainly from magnetic rather than electric effects. The complex permittivity
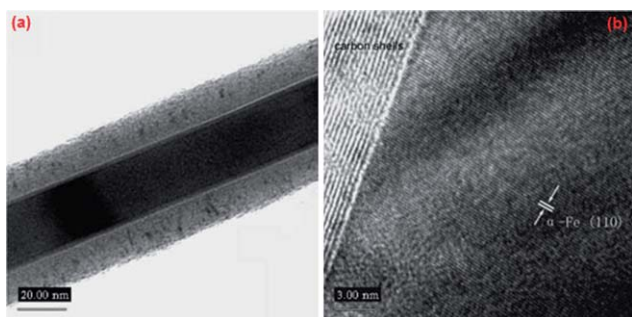
Fig. 28 (a) TEM image of Fe nanowires encapsulated within MWCNTs and (b) HRTEM image of crystalline α-Fe filled into the carbon shell. (Reprinted with permission from John Wiley and Sons.)[269]

and permeability depend on both the shape and phase of the CNT/Fe nanocapsulates.

Since the complex fabrication processes of the magnetic-particle-doped CNTs are unfavorable for practical application of such absorbing nanocomposites, it is important to search for other kinds of absorbing nanocomposites. Recent interest has been devoted to metal oxides containing nanomaterials (*e.g.* ZnO, SiO_2, *etc.*), which can be used as highly efficient microwave-absorbing materials due to the complex permittivity and permeability. It is easy to realize large scale synthesis of ZnO-containing nanomaterials for commercial applications with very low fabrication costs. Cao *et al.*[278] reported that cage-like ZnO/SiO_2 nanocomposites exhibit a relatively strong attenuation of microwaves in the X band, which is related to the unique geometrical morphology of the cage-like ZnO nanostructures. Zhou *et al.*[285] showed that the composite coatings containing ZnO whiskers have a good efficiency of microwave absorption. Chen *et al.*[286] reported that the ZnO nanowire–PS composites are strong absorption materials for microwaves in the X band, which is attributed to interfacial multipoles at the interface between the PS and the ZnO nanowires and to a high specific surface area.

SiO_2 is another promising shell material in fabricating the microwave absorbents, *e.g.* $SiO_2@FeNi_3$,[287] $Co_{50}@(SiO_2)_{50}$,[272]

barium ferrites@SiO_2,[288] and single-crystal α-iron oxide@$nSiO_2@mSiO_2$,[289] $Fe@SiO_2$,[113] *etc.* In a recent report, Guo *et al.*[289] synthesized a unique hematite/SiO_2/mesoporous silica ($FO@nSiO_2@mSiO_2$) core–shell nanocomposite, which possesses a broader absorption frequency and more tunable electromagnetic interference (EMI) shielding efficiency than those of the pure hematite. The intermediate nonporous silica layer was coated first *via* a sol–gel process, and then the mesoporous silica structure was coated as the outer shell layer by a surfactant-assembly method. SEM and TEM images in Fig. 29 show that the $FO@nSiO_2@mSiO_2$ composites possess distinct two-layer coating core–shell structures with ordered hexagonal mesostructure in the outer silica shell layer.

Fig. 30 shows that when the mesoporous silica layer is deposited on the surface of the $FO@nSiO_2$ composites, the $FO@nSiO_2@mSiO_2$ composites show the maximum RL value of −4.95 dB at 15.80 GHz, indicating an obvious shift towards the low frequency range. Compared with the FO particles and the one-layer core–shell $FO@nSiO_2$ composites, the multi-layer core–shell mesoporous composites $FO@nSiO_2@mSiO_2$ display better EMI shielding effectiveness and more RL. The RL can increase by about 50%, clearly indicating an improved EMI. The excellent EMI shielding effectiveness was attributed to the unique silica mesostructure.[289]

Traditional microwave shielding and absorbing materials such as metals and magnetic materials possess good mechanical and shielding property but display disadvantages such as being heavy, corrosive and poor processibility. Conductive polymers are widely studied for this application because of their foremost properties such as high conductivity to weight ratio, corrosion resistance and facile processibility.[290] Various conductivities with radiation frequency have made them useful in the radar absorbing materials,[291] among which polyaniline (PANI) is perhaps the most versatile because of its desirable properties, such as thermal and chemical stability, controllable conductivity and high conductivity at microwave frequencies.[292] By incorporation of the dielectric and magnetic fillers, the values of dielectric permittivity and magnetic permeability of such materials can be altered to

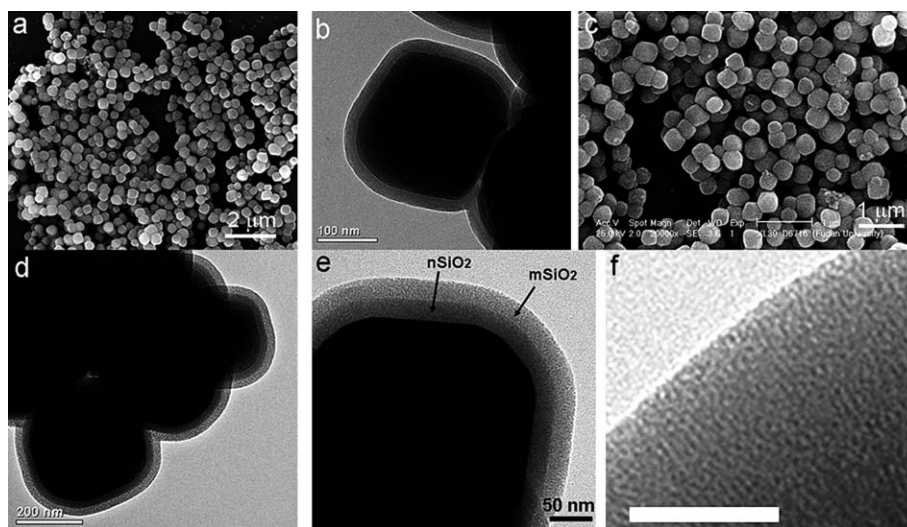**Fig. 29** (a) SEM image and (b) TEM image of $FO@nSiO_2$ core–shell structure, (c) SEM image, (d) TEM image and (e) HRTEM image of the $FO@nSiO_2@mSiO_2$ core–shell structure, (f) TEM image of the outer mesoporous layer from (e), the scale bar is 15 nm.[289]
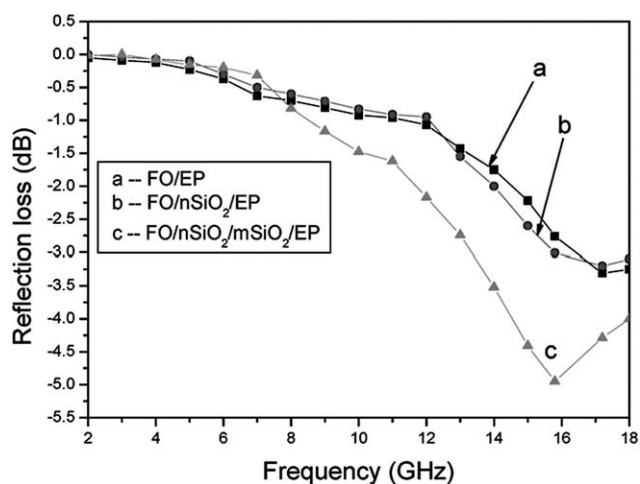
Fig. 30 Frequency dependent RL of the FO-based samples with component and structure variation: (a) FO/EP, (b) FO@nSiO$_2$@/EP, and (c) FO@nSiO$_2$@mSiO$_2$/EP.[289]

achieve maximum absorption of the electromagnetic energy. Phang et al.[293] synthesized a novel PANI/dopant/TiO$_2$/CNT nanocomposite with excellent microwave absorbing and shielding performance. TiO$_2$ and CNT are the dielectric and magnetic fillers, which enhance the dielectric and magnetic properties of PANI. In addition, hexanoic acid (HA) is the dopant used to improve the conductivity of PANI. PANI/HA/TiO$_2$/SWNT with 20% of SWNT exhibits the best microwave absorption property (∼99.2% absorption) with an RL of −21.7 dB at 6 GHz due to its moderate conductivity (1.27 S cm^{-1}), magnetization (M_s = 1.01 emu g^{-1}), highest tan δ and heterogeneity.

Besides PANI, polypyrrole (PPy) and poly (3,4-ethylenedioxy thiophene) (PEDOT) are other promising candidates. Li et al.[294] synthesized Fe$_3$O$_4$/PPy core/shell nanocomposites, with Fe$_3$O$_4$ NPs as the core and PPy as the shell via in situ chemical oxidative polymerization of pyrrole monomers on the surface of Fe$_3$O$_4$ NPs. The electromagnetic characteristics of Fe$_3$O$_4$/PPy core/shell nanocomposites were investigated with a vector network analyzer in the 2–18 GHz range. The absorbing peak position moves to lower frequency with increasing the thicknesses of samples. The value of the minimum RL is −22.4 dB at 12.9 GHz for Fe$_3$O$_4$/PPy core/shell nanocomposites with a thickness of 2.3 mm, and a broad peak with a bandwidth lower than −10 dB is about 5 GHz. Such strong absorption is attributed to better electromagnetic matching due to the existence of PPy and the special core/shell structure. Ohlan et al.[295] reported the complex permittivity, permeability, and microwave absorption properties of core shell type PEDOT nanocomposites with barium ferrite (BaF) in the 12.4–18 GHz frequency range. These nanocomposites showed strong microwave absorption with an SE$_A$ value of 22.5 dB at 15 GHz with minimal RL of 2 dB. The high absorption properties mainly result from the high dielectric and magnetic losses in the composites and depend on the concentration of barium ferrite in the polymer composites.

4.4 Biomedical applications

Due to the unique configuration, the core–shell structured particles play increasing roles in biomedical applications, which include biomedical imaging therapeutics, drug delivery, gene delivery, separation and purification of proteins, cancer, etc.[296–299]

Metal nanoshells, typically gold, possess highly favorable optical and chemical properties, which can be used for biomedical imaging and therapeutic applications.[300] The normally used metal nanoshells for biological applications include the NPs composed of a dielectric core such as silica coated with an ultrathin metallic layer. The reported shell usually is Au. As compared with the pure colloidal Au NPs possessing a brilliant red color which have been used in the consumer-related medical products, such as home pregnancy tests, the Au nanoshell possesses a tunable optical property depending dramatically on the relative size of the core and the thickness of the shell, which can be varied across a wide range from visible to near infrared spectral regions. Coupled with the biocompatibility and easy bioconjugation, the optical properties of the nanoshells render these nanoshell materials highly suitable for targeted bioimaging and therapeutic applications. In addition, the hollow carbon nanocapsules have the potential applications in the delivery, protection of protein and enzymes and magnetic particles from oxidation, design of radioactive NPs for radiology, radiation therapy and sensing.[301] While switching the core materials from dielectric to magnetic, the nondestructive magnetic field can be used as a stimulant for the targeting drug delivery, controlled release or biosensors. The Au shell can be biofunctionalized with other organic molecules such as through the thiol chemistry. With the aid of a magnetic field, the possible biosensors for detecting the molecule targeting sites can be developed.

Microcapsules have been reported to be an effective way to encapsulate, transport and control drug, mineral, and protein release.[129,302–306] Due to the magnetic property, magnetic NPs can be used for drug delivery under the external magnetic field stimulus.[307–309] Compared with the change of the pH value, solution ionic strength, and adding organic solvent to achieve the delivery of the materials, the stimulating magnetic field in the incorporation of Co–Au NPs embedding capsules has the following advantage: the compatibility with the physiological conditions of the human body. Due to the fact that water was used to remove the polyelectrolyte during the layer-by-layer assembly capsule fabrication process, the zero-valence metallic NPs without a protecting shell would lose/degrade much of their magnetic property. The layer-by-layer assembly method for the capsule fabrication was described in detail elsewhere.[310] The incorporation of the Co–Au core–shell NPs was also followed by the layer-by-layer assembly method through the adsorption of the small size NPs onto the surface of the substrate core. With the incorporation of noble metal shell, the zero-valence metallic magnetic NPs were successfully incorporated into the capsule walls by surviving from the electrolyte solution.[129] Fig. 31 shows the schemes of the capsule fabrication and the magnetic field effect on the FITC–dextran diffusion into the capsules through the walls. Fluorescein isothiocyanate (FITC)–dextran (M_W 2 000 000) successfully permeated into the empty capsules under the stimulating effect of an alternating electromagnetic field on the capsule FITC–dextran solution. The permeability effect was characterized by the confocal laser scanning microscopy (CLSM) and the ratio of the fluorescence intensities inside and outside of the capsules was employed as a parameter to express the permeability. Fig. 32 shows the confocal images of the capsules
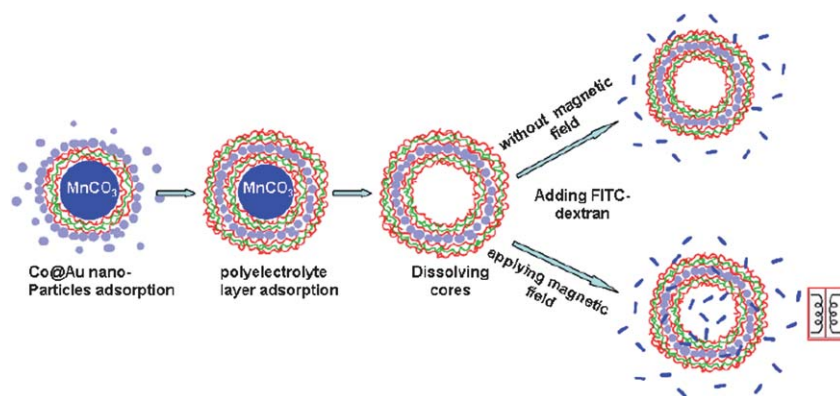
Fig. 31 Scheme of capsule fabrication and the effect of magnetic field on the FITC–dextran diffusion through the wall. (Reprinted with permission from American Chemical Society.)[129]

mixed with the FITC-labeled dextran (M_W 2 000 000, pH 7.5, 1 mg mL^{-1}) and their corresponding fluorescence intensity profiles. The dark interior of the capsule was observed even after one hour mixing with the FITC-labeled dextran solution. The brighter image of the interior capsules was observed after half an hour mixing within the FITC-labeled dextran solution, indicating that most of the FITC-labeled dextran was diffused into the capsules under the effect of the magnetic field. The lower fluorescence intensity and the higher fluorescence intensity in the interior without and with the applied field, the bottom of Fig. 32 (a) and (b), indicate that the FITC-labeled dextran is blocked from diffusion into the capsules without the field and FITC-labeled dextran is diffused into the capsules with an applied magnetic field indicating that the magnetic field has an effect on the diffusion into the capsules.[129]

In addition to drug delivery, the core–shell structured NPs have also been designed for the gene delivery. Lu *et al.*[311] fabricated "peas in a pod"-like assemblies of Co@Au yolk/shell nanospheres under an external magnetic field, Fig. 33. Owing to their cavitary

Fig. 32 Confocal image of magnetic capsules mixed with FITC–dextran (a) without magnetic field and (b) after applying an alternating magnetic field for half hour, and the corresponding optical density profiles are shown below. (Reprinted with permission from American Chemical Society.)[129]

structure and positive surface potential, these hybrid yolk/shell nanostructures show excellent performance in the applications as a nonviral vector for gene delivery and transfection.

The efficient separation and purification of the proteins has become essentially important for the recent advancements in the biomedical and pharmaceutical research. Among various technologies, the selective adsorption technology, which relies on the specific interactions between proteins and absorbent (*e.g.* the formation of a flexible polymer chain–protein complex) to extract the targeted (desired or undesired) protein from its mixture, is promising. For this purpose, Shao *et al.*[312] prepared submicron-size superparamagnetic Fe$_3$O$_4$@silica-*g*-PAA microspheres for the selective absorption and separation of lysozyme. Due to the high density of the reactive functional groups, the binding capacity of the Fe$_3$O$_4$@silica-*g*-PAA microspheres for lysozyme was 22 times as much as that of pure Fe$_3$O$_4$@silica microspheres at the same pH condition. A maximum binding capacity of 127 mg g^{-1} was achieved. The magnetic Fe$_3$O$_4$@silica-*g*-PAA microspheres could not only be manipulated magnetically but also exhibited fast adsorption and desorption rates due to the high magnetic content and the absence of internal diffusion resistance. Besides, the Fe$_3$O$_4$@silica-*g*-PAA microspheres could selectively separate lysozyme from the binary protein mixture of lysozyme and ovalbumin. Consequently, such core–shell type protein absorbents may lead the selective adsorption technology to significantly lower costs and energy savings compared with the routine approaches.

Gao *et al.*[313] synthesized FePt@CoS$_2$ yolk–shell nanocrystals by the mechanism of the Kirkendall effect where the FePt NPs serve as the seeds as a potent agent to kill HeLa cells. The illustrated possible mechanism is shown in Fig. 34. After the cellular uptake, under the acidic environment inside the secondary lysosomes, FePt cores are oxidized and destroyed to become metal ions because the reactivity of the unprotected iron promotes the disintegration of FePt to release platinum ions (Pt^{2+}). The permeability (or the rupture) of the CoS$_2$ shells allows these Pt^{2+} ions to diffuse out of the shells easily, enter into the nucleus and mitochondria, damage the DNA double-helix chains by coordinating with 5′-GG-3′ bases of DNA, and lead to the apoptosis of the HeLa cells. The cytotoxicity of the FePt@CoS$_2$ yolk–shell nanocrystals, evaluated by the MTT assay (a standard colorimetric assay which measures the changes in color for
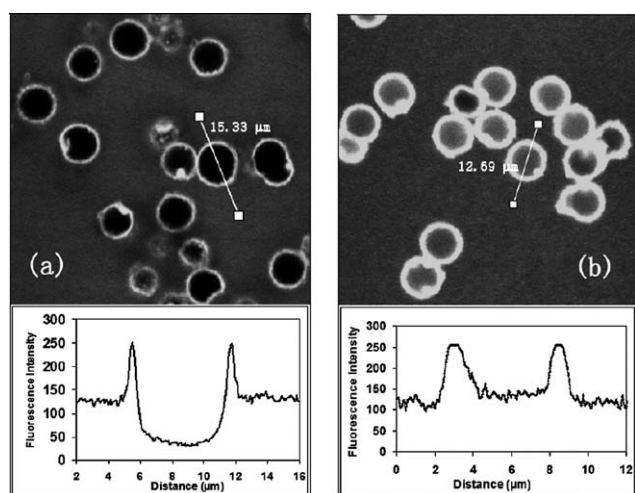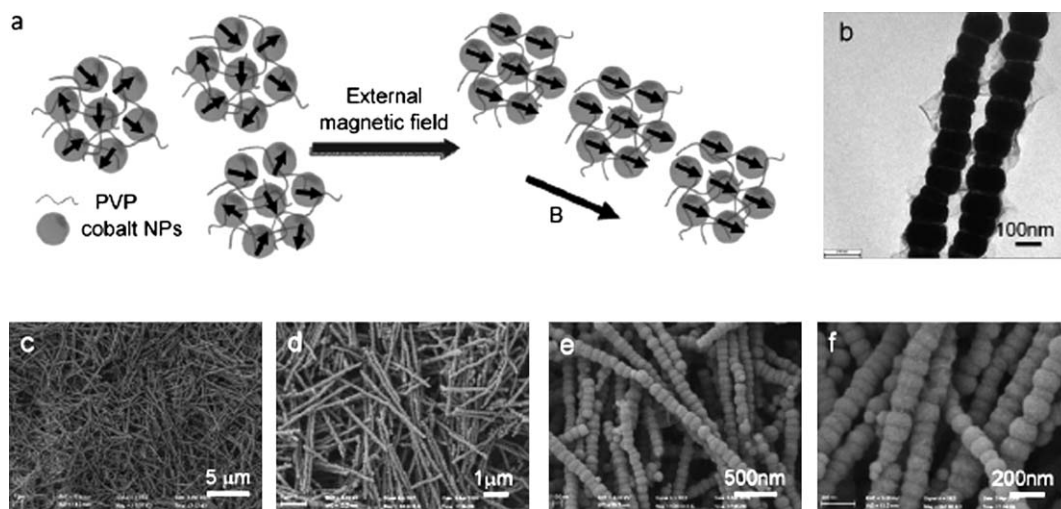
Fig. 33 (a) Schematic illustration of the formation of "peas in a pod"-like assemblies from nanospheres. (b) TEM image and (c–f) a series of SEM images of the large-scale synthesized uniform pea-like assemblies of Co@Au yolk/shell nanospheres. (Reprinted with permission from John Wiley and Sons.)[311]

measuring cellular amount), shows a much lower IC50 (35.5 ± 4.7 ng of Pt per mL for HeLa cell) than that of cisplatin (230 ng of Pt per mL). These results are significant because almost none of the platinum-based complexes produced for clinical trials in the past 3 decades have shown higher activity than that of the parent drug, cisplatin. The exceptionally high toxicity of FePt@CoS$_2$ yolk–shell nanocrystals (about 7 times higher than that of cisplatin in terms of Pt) may lead to a new design of an anticancer nanomedicine.
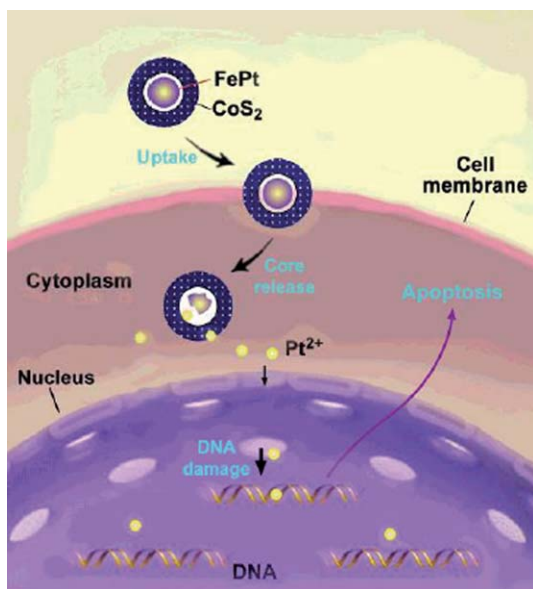

Fig. 34 Scheme of a possible mechanism accounting for the FePt@CoS$_2$ yolk–shell nanocrystals killing HeLa cells. After cellular uptake, FePt NPs were oxidized to give Fe^{3+} (omitted for clarity) and Pt^{2+} ions (yellow). The Pt^{2+} ions enter into the nucleus (and mitochondria), bind to DNA, and lead to apoptosis of the HeLa cell. (Reprinted with permission from American Chemical Society.)[313]

4.5 Environmental remediation application

With the rapidly increased concerns on the environmental health, there are a few papers reporting the application of core–shell structures in environmental remediation, particularly in water treatment, *e.g.* the removal of organic pollutants, heavy metals, and microcystins, *etc.* Generally, such core–shell structures should at least possess a high specific surface area shell for the adsorption purpose and a magnetic core for the separation purpose. Transition metal oxides can be used both as absorbents to remove organic waste from water and as catalysts in subsequent catalytic combustion at a relatively low temperature. Fei *et al.*[314] have successfully synthesized micrometre-scale manganese oxide hierarchical hollow nanostructures, which displayed a good ability in removing contamination (*e.g.* Congo red). The high cost of the materials is a major drawback for the practical applications, so synthesis of materials with low cost, high adsorption abilities and easy recycling can retrench the cost in wastewater treatment.

Zhai *et al.*[315] developed a method to construct ordered magnetic core–manganese oxide shell nanostructures by simply mixing manganese ferrite NPs and potassium permanganate without any additional modification of the core. Two-dimensional nanostructures of manganese oxides have grown on the magnetic cores to constitute three-dimensional ordered structures, the inset of Fig. 35(A). It was found that the existence of Mn in the core had a significant effect on the fabrication of the symmetrical manganese oxide shell. Additionally, the as-prepared magnetic materials had a strong magnetic force, which can be magnetically separated effectively. The as-prepared ordered magnetic core–manganese oxide shell NPs were used as absorbents in wastewater treatment and Congo red was chosen as a typical organic pollutant. The characteristic UV-vis absorption of Congo red at 500 nm was chosen for monitoring the adsorption process. When 90 mg adsorbent was used in 50 mL (80 mg L^{-1}) Congo red solution, over 85% of the Congo red can be removed within 60 min at room temperature, Fig. 35
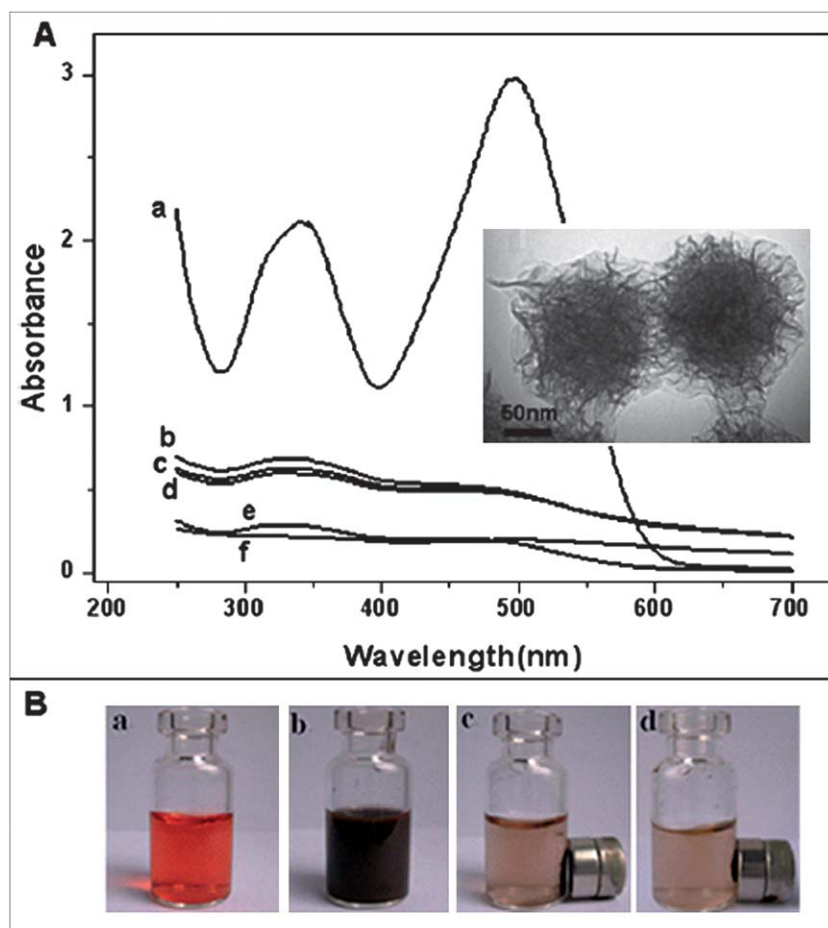
Fig. 35 (A) Absorption spectra of a solution of Congo red in the presence of ordered magnetic core–manganese oxide shell nanoparticles at different times: (a) 0 min; (b) 5 min; (c) 20 min; (d) 60 min; (e) 60 min after centrifugation and (f) 12 h; the inset shows the TEM image of the synthesized magnetic core–manganese oxide shell nanoparticles. (B) Photos of absorption of congo red with different times by ordered magnetic core–manganese oxide shell nanoparticles: (a) 0 min; (b) after mixing with the magnetic absorbents; (c) 5 min; (d) 30 min.[315]

(A). Curve b in Fig. 35(A) indicates that most of the Congo red has been adsorbed after 5 min. A clear change in the concentration of Congo red can also be observed by the photographs recorded at different times, Fig. 35(B). Similarly, boehmite hollow core/shell and hollow microspheres prepared by Cai *et al.*[316] also showed a high adsorption affinity toward organic pollutants in water.

In some chemical processes, for example, organic synthesis, synthetic fiber, textile processing, wood processing, and painting, formaldehyde has often been emitted. Because of the large water-solubility of formaldehyde, the wastewater of these chemical processes generally contains the low concentration formaldehyde (0.2–4.0 g L^{-1}), and sometimes even more than 10 g L^{-1}. It brings great harm to the environment and human beings.[317] Hence, an effective way for the elimination of formaldehyde in the industrial wastewater is particularly necessary. Ji *et al.*[318] synthesized core–shell structured Cu/Fe$_3$O$_4$@SiO$_2$ microsphere catalysts *via* a two-step method. At first, the Fe$_3$O$_4$@SiO$_2$ microspheres were synthesized using the nano-Fe$_3$O$_4$ as the core, tetraethyl orthosilicate (TEOS) as the silica source, and cetyl trimethyl ammonium bromide (CTAB) as a surfactant. Secondly, the Cu nanograins, obtained by reducing copper ammonia complexes with hydrazine hydrate, were supported on the surface of the

Fe$_3$O$_4$@SiO$_2$ microspheres, Fig. 36. The surface embedded Cu NPs are the active sites for the low-concentration formaldehyde conversion to H$_2$ under mild reaction conditions. Since the Cu NPs assemble on the surface of Fe$_3$O$_4$@SiO$_2$, the agglomeration of the Cu NPs can be easily prevented. At the same time, the catalysts can also be effectively separated and reused under a magnetic field due to the presence of the Fe$_3$O$_4$ cores. The observations indicated that the catalyst with 15 wt% of Cu exhibited the best catalytic activity and the accumulative generation amount of H$_2$ reached 42 mL in 45 min. After recycling for 8 times, the catalyst still exhibited high catalytic activity.

Compared to other shells, carbon exhibits much higher stability in harsh environments such as acidic or basic media[319,320] and better biocompatibility.[321] Regular shape and narrow particle size distribution are necessary to maintain the dispersion stability of the NPs in the solvents. The large specific surface area of the carbon shell has the advantage to enhance the pollutant treatment efficiency. Additionally, the mobility of the magnetic NPs will enhance the treament ability and facilitate the nanoparticle recycling after pollutant treatment with an introduced external magnetic field.

In this section, the applications of carbon shell in the heavy metal removal and weakly biodegradable pollutants from the
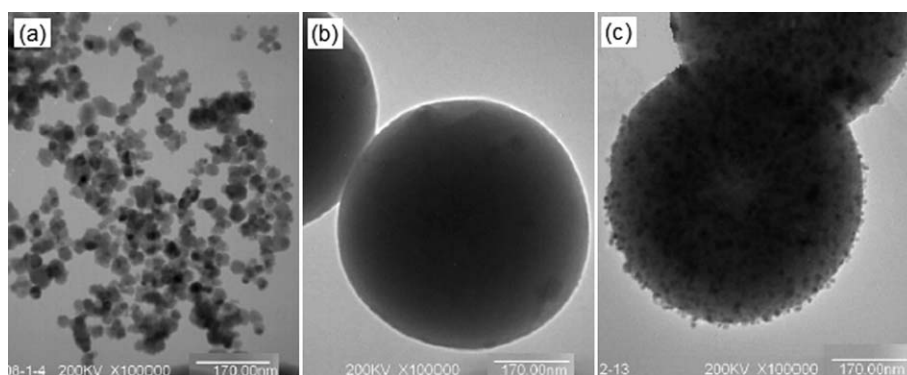
Fig. 36 TEM images of (a) Fe_3O_4 particles, (b) $Fe_3O_4@SiO_2$ magnetic microspheres, and (c) 15% $Cu/Fe_3O_4@SiO_2$ catalyst. (Reprinted with permission from Elsevier.)[318]

polluted water are illustrated. Hexavalent chromium Cr(VI) is a commonly identified contaminant in soils and groundwater because of its high toxicity and mobility.[322] The maximum permissible limit of total chromium in the drinking water has been recommended as 0.1 mg L^{-1} by the US Environmental Protection Agency (EPA).[323] A variety of methods have been developed to remove Cr(VI) from wastewater such as solvent extraction, ion exchange, osmosis, chemical precipitation, membrane separation and adsorption.[324,325] Although these methods are efficient for Cr (VI) removal, the cost is relatively high.[326] Consequently, an alternative adsorption is favorable and feasible because of its low-cost and high efficiency.[327,328] Besides, adsorption can effectively reduce heavy metals at low concentrations in wastewater when compared with the chemical precipitation and electrochemical methods.[329,330] Activated carbon prepared from coconut wood, lignin, petroleum and coke is one of the absorbents being used to purify polluted water.[331,332] However, activated carbon has not been able to reduce the concentration of contaminants at ppb (part per billion) levels.[333] Sun et al.[334] have also reported on the removal of weakly biodegradable methyl orange by carbon-encapsulated magnetic NPs.

Recently, Guo et al.[107] have developed a facile way to fabricate carbon coated Fe NPs from solid state chemistry with iron nitrate as the iron precursor, inexpensive sodium chloride as the spacer, and poly(vinyl alcohol) as the carbon precursor. A solid rather than porous structure is observed by HRTEM and acidic test. The removal of heavy metals by these hybrid materials is found to be a physical adsorption rather than the redox between Fe and heavy metal ions. Fig. 37 shows the adsorption process of the heavy metal removal.

Sun et al.[334] have reported the removal of a weakly biodegradable methyl orange (MO) by using porous sphere composites made of carbon and magnetic NPs. This ability to remove the pollutants was found to be effective even after four cycles of adsorption and desorption tests. Fig. 38 shows the scheme of the MO removal process.

Microcystins (MCs) such as MC-RR, MC-YR, and MC-LR are disocyclic heptapeptides with molecular weights of about 1000 Da. MCs are extremely toxic and are produced in the cyanobacterial blooms widely occurring in many eutrophic waters. Conventional approaches such as coagulation and sand filtration are effective for the removal of the particulate cyanobacterial cells but not for the dissolved toxins. Activated carbon can be used to
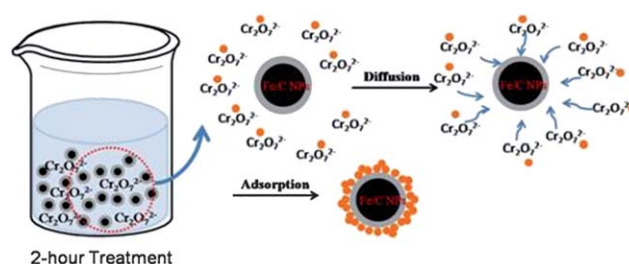

Fig. 37 Schematic adsorption process of the heavy metal removal by C coated Fe NPs.[107]

remove MCs, but it requires large carbon doses due to the deficiency of the accessible mesopores for the adsorption of large MCs.[335] Chlorination and ozonation could be used to remove MCs, but the required high dosage may result in the formation of carcinogenic substances.[336] Biological methods require a relatively long reaction time and are thus not feasible.[337] To address these problems, Deng et al.[338] synthesized a sandwich structure with a magnetite core, a nonporous silica layer in the middle layer, and an ordered mesoporous silica phase with cylindrical channels in the outer layer. The synthesis procedure and the corresponding TEM and SEM images of the particles in each step are shown in Fig. 39. Interestingly, the mesopore channels are found to be perpendicular to the microsphere surface. The unique microstructures of the obtained microspheres make it a suitable absorbent for MCs. First, the middle nonporous silica layer could protect the magnetite from etching in harsh application occasions. Second, the mesoporous silica shell not only offers high specific surface area for the derivation of numerous functional groups but also provides large accessible pore volume for the adsorption and encapsulation of the biomacromolecules and even functional NPs (e.g., quantum dots). Notably, due to their unique perpendicular orientation, the mesopore channels of the microspheres are readily accessible, favoring the adsorption and release of the large guest objects triggered by an external stimulus. With this novel absorbent, the authors achieved extremely high removal efficiencies of 95.4% for MC-RR, 97.2% for MC-YR, and 97.5% for MC-LR within 60 s. Additionally, after extraction of the trapped MCs with acetonitrile/water mixture, the microspheres can be reused with an MC removal efficiency higher than 90% even after being used for eight times.
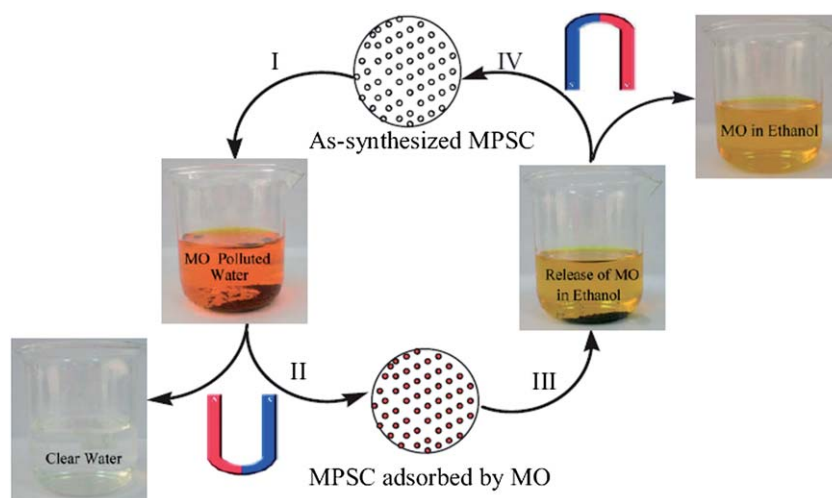
Fig. 38 Proposed scheme for the removal of pollutants in water by magnetically mobilizing the porous magnetic composite sample: (I) the magnetic composite is added into water polluted with MO to adsorb the pollutants; (II) the magnetic composite with adsorbed MO is separated from water by a magnetic field, giving clear water; (III) the magnetic composite with adsorbed pollutants is transferred into ethanol to release the pollutants; (IV) after almost complete desorption of the pollutants in ethanol, the regenerated magnetic composite is separated again by a magnetic field and can be used once more to adsorb pollutants. (Reprinted with permission from John Wiley and Sons.)[334]

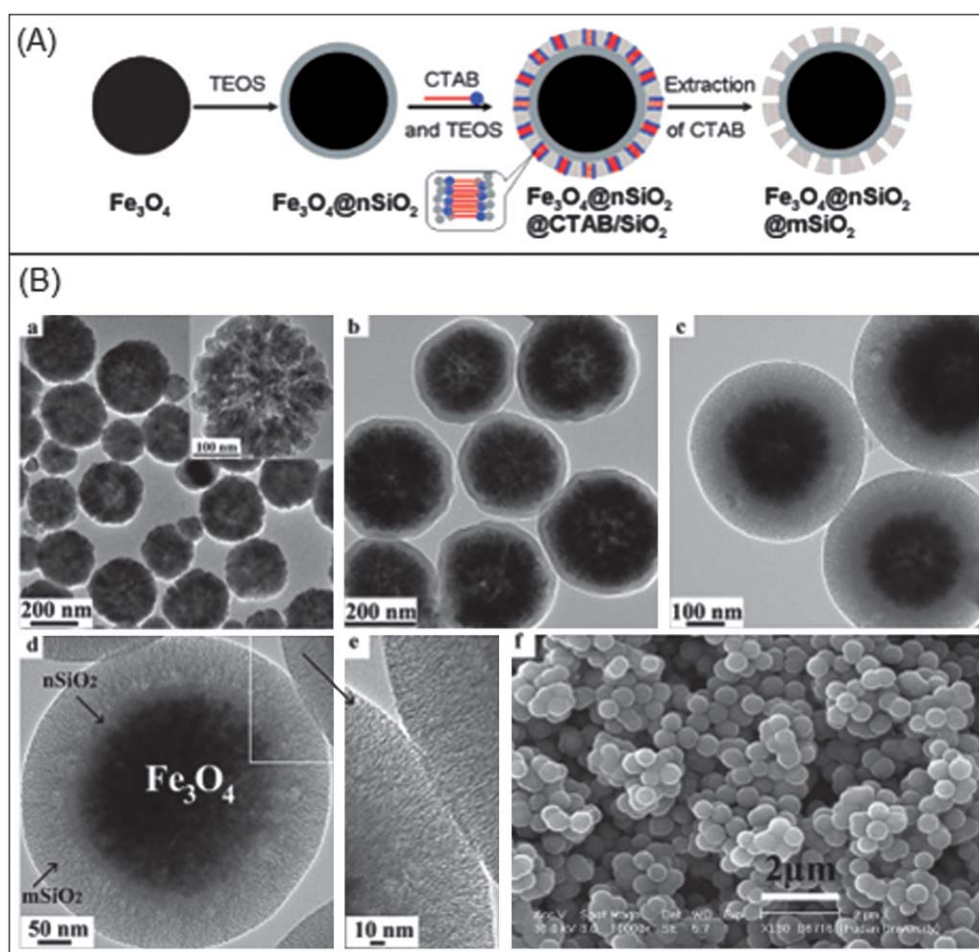**Fig. 39** (A) The formation of $Fe_3O_4@nSiO_2@mSiO_2$ microspheres; (B) TEM images of (a) Fe_3O_4 particles, (b) $Fe_3O_4@nSiO_2$, (c–e) $Fe_3O_4@n$-$SiO_2@mSiO_2$ microspheres, and (f) SEM image of $Fe_3O_4@nSiO_2@mSiO_2$ microspheres. (Reprinted with permission from American Chemical Society.)[338]

5. Conclusion, challenges and future trend

In this review, various fabrication approaches to create a shell around the magnetic core NPs with different shell materials were presented. The fabrication methods were classified into different categories for the sake of simplicity. The effects of various shells on the physical and chemical properties of the core–shell nanoparticles were analyzed. The possible applications of core–shell NPs in catalysis, GMR sensor, electromagnetic radiation shielding, biomedical field and environmental remediation have been described. A comprehensive summary of the synthetic methods and properties of core–shell NPs with relevant literature references has been presented for the first time.

The wide potential applications of the core–shell nanoparticles are predicted and are currently limited by the availability of large quantities of these multifunctional nanoparticles. Methods for large-scale production are demanding in order to achieve the required porous or solid shell structures. The structural and physical property compatibility between the core and shell structural materials is rarely studied and is very important in determining the stability of the whole unit. For example, different values of the coefficient of thermal expansion (CTE) between the core and shell will cause poor adhesion or cause sintering to form alloys, which will limit these nanoparticles to be applied in conditions requiring operations at high temperatures or a broad temperature range. To improve the quality of the core–shell nanoparticles is another trend of future research.

Acknowledgements

References

1 S. Gangopadhyay, G. C. Hadjipanayis, S. I. Shah, C. M. Sorensen, K. J. Klabunde, V. Papaefthymiou and A. Kostikas, *J. Appl. Phys.*, 1991, **70**, 5888.
2 S. N. Khanna and S. Linderoth, *Phys. Rev. Lett.*, 1991, **67**, 742.
3 S. Gangopadhyay, G. C. Hadjipanayis, B. Dale, C. M. Sorensen, K. J. Klabunde, V. Papaefthymiou and A. Kostikas, *Phys. Rev. B: Condens. Matter Mater. Phys.*, 1992, **45**, 9778.
4 D. Farrell, S. A. Majetich and J. P. Wilcoxon, *J. Phys. Chem. B*, 2003, **107**, 11022.
5 C. B. Murray, S. Sun, H. Doyle and T. Betley, *MRS Bull.*, 2001, **26**, 985.
6 J. P. Chen, C. M. Sorensen, K. J. Klabunde and G. C. Hadjipanayis, *J. Appl. Phys.*, 1994, **76**, 6316.
7 J. P. Chen, K. M. Lee, C. M. Sorensen, K. J. Klabunde and G. C. Hadjipanayis, *J. Appl. Phys.*, 1994, **75**, 5876.
8 J. Osuna, D. de Caro, C. Amiens, B. Chaudret, E. Snoeck, M. Respaud, J.-M. Broto and A. Fert, *J. Phys. Chem.*, 1996, **100**, 14571.
9 O. Kitakami, H. Sato, Y. Shimada, F. Sato and M. Tanaka, *Phys. Rev. B: Condens. Matter Mater. Phys.*, 1997, **56**, 13849.
10 X. M. Lin, C. M. Sorensen, K. J. Klabunde and G. C. Hadjipanayis, *Langmuir*, 1998, **14**, 7140.
11 C. Petit, A. Taleb and M. P. Pileni, *J. Phys. Chem. B*, 1999, **103**, 1805.
12 S. H. Sun and C. B. Murray, *J. Appl. Phys.*, 1999, **85**, 4325.
13 D. P. Dinega and M. G. Bawendi, *Angew. Chem., Int. Ed.*, 1999, **38**, 1788.
14 V. F. Puntes, K. M. Krishnan and A. P. Alivisatos, *Science*, 2001, **291**, 2115.
15 H. Bonnemann, W. Brijoux, R. Brinkmann, N. Matoussevitch, N. Waldofner, N. Palina and H. Modrow, *Inorg. Chim. Acta*, 2003, **350**, 617.
16 V. F. Puntes, D. Zanchet, C. K. Erdonmez and A. P. Alivisatos, *J. Am. Chem. Soc.*, 2002, **124**, 12874.
17 G. N. Glavee, K. J. Klabunde, C. M. Sorensen and G. C. Hadjipanayis, *Langmuir*, 1993, **9**, 162.
18 S. E. Apsel, J. W. Emmert, J. Deng and L. A. Bloomfield, *Phys. Rev. Lett.*, 1996, **76**, 1441.
19 N. Cordente, C. Amiens, B. Chaudret, M. Respaud, F. Senocq and M. J. Casanove, *J. Appl. Phys.*, 2003, **94**, 6358.
20 Y. Hou and S. Gao, *J. Mater. Chem.*, 2003, **13**, 1510.
21 M. Green and P. O'Brien, *Chem. Commun.*, 2001, 1912.
22 M. P. Zach and R. M. Penner, *Adv. Mater.*, 2000, **12**, 878.
23 T. O. Ely, C. Amiens, B. Chaudret, E. Snoeck, M. Verelst, M. Respaud and J.-M. Broto, *Chem. Mater.*, 1999, **11**, 526.
24 C. Estournes, T. Lutz, J. Happich, T. Quaranta, P. Wissler and J. L. Guille, *J. Magn. Magn. Mater.*, 1997, **173**, 83.
25 P. Zhang, F. Zuo, F. K. Urban, A. Khabari, P. Griffiths and A. Hosseini-Tehrani, *J. Magn. Magn. Mater.*, 2001, **225**, 337.
26 I. M. L. Billas, A. Chatelain and W. A. de Heer, *Science*, 1994, **265**, 1682.
27 S. P. Gubin and Y. A. Koksharov, *Inorg. Mater.*, 2002, **38**, 1085.
28 R. K. Rana, Y. Koltypin and A. Gedanken, *Chem. Phys. Lett.*, 2001, **344**, 256.
29 H. Ago, J. Qi, K. Tsukagoshi, K. Murata, S. Ohshima, Y. Aoyagi and M. Yumura, *J. Electroanal. Chem.*, 2003, **559**, 25.
30 Y. Lu, Z. Zhu and Z. Liu, *Carbon*, 2004, **42**, 361.
31 M. Lu, W.-M. Liu, X.-Y. Guo and H.-L. Li, *Carbon*, 2004, **42**, 805.
32 Y. Huh, J. Y. Lee, S. K. Choi and C. J. Lee, *Mater. Res. Soc. Symp. Proc.*, 2003, **788**, 515.
33 N. S. Kim, S. Y. Bae and J. Park, *Mater. Res. Soc. Symp. Proc.*, 2003, **800**, 105.
34 Y.-T. Jang, J.-H. Ahn, Y.-H. Lee and B.-K. Ju, *Chem. Phys. Lett.*, 2003, **372**, 745.
35 S.-W. Kim, S. U. Son, S. S. Lee, T. Hyeon and Y. K. Chung, *Chem. Commun.*, 2001, 2212.
36 S. U. Son, K. H. Park and Y. K. Chung, *J. Am. Chem. Soc.*, 2002, **124**, 6838.
37 M. Moreno-Manas and R. Pleixats, *Acc. Chem. Res.*, 2003, **36**, 638.
38 K. H. Park, S. U. Son and Y. K. Chung, *Org. Lett.*, 2002, **4**, 4361.
39 S. U. Son, K. H. Park and Y. K. Chung, *Org. Lett.*, 2002, **4**, 3983.
40 C. B. Murray, S. H. Sun, W. Gaschler, H. Doyle, T. A. Betley and C. R. Kagan, *IBM J. Res. Dev.*, 2001, **45**, 47.
41 F. Fettar, S. F. Lee, F. Petroff, A. Vaures, P. Holody, L. F. Schelp and A. Fert, *Phys. Rev. B: Condens. Matter Mater. Phys.*, 2002, **65**, 174415.
42 B. M. Berkovsky, V. F. Medvedev and M. S. Krakow, *Magnetic Fluids: Engineering Applications*, Oxford University Press, Oxford, 1993.
43 S. P. Gubin, Y. I. Spichkin, Y. A. Koksharov, G. Y. Yurkov, A. V. Kozinkin, T. I. Nedoseikina, M. S. Korobov and A. M. Tishin, *J. Magn. Magn. Mater.*, 2003, **265**, 234.
44 V. F. Puntes, P. Gorostiza, D. M. Aruguete, N. G. Bastus and A. P. Alivisatos, *Nat. Mater.*, 2004, **3**, 263.
45 K. V. P. M. Shafi, A. Gedanken and R. Prozorov, *Adv. Mater.*, 1998, **10**, 590.
46 M.-P. Pileni, *Adv. Funct. Mater.*, 2001, **11**, 323.
47 G. X. Chen, M. H. Hong, B. Lan, Z. B. Wang, Y. F. Lu and T. C. Chong, *Appl. Surf. Sci.*, 2004, **228**, 169.
48 M. Z. Rong, M. Q. Zhang, H. B. Wang and H. M. Zeng, *J. Polym. Sci., Part B: Polym. Phys.*, 2003, **41**, 1070.
49 M. Z. Rong, M. Q. Zhang, H. B. Wang and H. M. Zeng, *Appl. Surf. Sci.*, 2002, **200**, 76.
50 C. Castro, J. Ramos, A. Millan, J. Gonzalez-Calbet and F. Palacio, *Chem. Mater.*, 2000, **12**, 3681.
51 A. Manna, T. Imae, M. Iida and N. Hisamatsu, *Langmuir*, 2001, **17**, 6000.
52 Z. Guo, L. L. Henry, V. Palshin and E. J. Podlaha, *J. Mater. Chem.*, 2006, **16**, 1772.
53 Z. Guo, S. Park, S. Wei, T. Pereira, M. Moldovan, A. B. Karki, D. P. Young and H. T. Hahn, *Nanotechnology*, 2007, **18**, 335704.

54 Z. Guo, K. Shin, A. Karki, D. Young, R. Kaner and H. Hahn, *J. Nanopart. Res.*, 2009, **11**, 1441.

55 J. Zhu, S. Wei, X. Chen, A. B. Karki, D. Rutman, D. P. Young and Z. Guo, *J. Phys. Chem. C*, 2010, **114**, 8844.

56 D. Zhang, R. Chung, A. B. Karki, F. Li, D. P. Young and Z. Guo, *J. Phys. Chem. C*, 2010, **114**, 212.

57 Z. Lu, M. D. Prouty, Z. Guo, V. O. Golub, C. S. S. R. Kumar and Y. M. Lvov, *Langmuir*, 2005, **21**, 2042.

58 J. H. J. Scott, Z. Turgut, K. Chowdary, M. E. McHenry and S. A. Majetich, *Mater. Res. Soc. Symp. Proc.*, 1998, **501**, 121.

59 Z. Turgut, N. T. Nuhfer, H. R. Piehler and M. E. McHenry, *J. Appl. Phys.*, 1999, **85**, 4406.

60 A. K. Giri, K. M. Chowdary and S. A. Majetich, *Mater. Phys. Mech.*, 2000, **1**, 1.

61 Z. H. Wang, C. J. Choi, J. C. Kim, B. K. Kim and Z. D. Zhang, *Mater. Lett.*, 2003, **57**, 3560.

62 X. Su, H. Zheng, Z. Yang, Y. Zhu and A. Pan, *J. Mater. Sci.*, 2003, **38**, 4581.

63 Q. Li, H. Li, V. G. Pol, I. Bruckental, Y. Koltypin, J. Calderon-Moreno, I. Nowik and A. Gedanken, *New J. Chem.*, 2003, **27**, 1194.

64 N. O. Nunez, P. Tartaj, M. P. Morales, R. Pozas, M. Ocana and C. J. Serna, *Chem. Mater.*, 2003, **15**, 3558.

65 N. O. Nunez, P. Tartaj, M. P. Morales, P. Bonville and C. J. Serna, *Chem. Mater.*, 2004, **16**, 3119.

66 C. de Julian, C. Sangregorio, G. Mattei, G. Battaglin, E. Cattaruzza, F. Gonella, S. Lo Russo, F. D'Orazio, F. Lucari, G. De, D. Gatteschi and P. Mazzoldi, *J. Magn. Magn. Mater.*, 2001, **226–230**, 1912.

67 N. Chakroune, G. Viau, C. Ricolleau, F. Fievet-Vincent and F. Fievet, *J. Mater. Chem.*, 2003, **13**, 312.

68 K. V. P. M. Shafi, A. Gedanken and R. Prozorov, *J. Mater. Chem.*, 1998, **8**, 769.

69 G. Mattei, C. de Julian Fernandez, P. Mazzoldi, C. Sada, G. De, G. Battaglin, C. Sangregorio and D. Gatteschi, *Chem. Mater.*, 2002, **14**, 3440.

70 B. Yang, Y. Wu, B. Zong and Z. Shen, *Nano Lett.*, 2002, **2**, 751.

71 Q.-Y. Wu, K. Fang, L.-l. Cui, S.-p. Li, J.-j. Yang and W.-m. Mao, *Qingdao Keji Daxue Xuebao, Ziran Kexueban*, 2003, **24**, 37.

72 C. J. Yang, K. S. Kim and J. Wu, *J. Appl. Phys.*, 2001, **90**, 5741.

73 D.-l. Lu, K. Domen and K.-i. Tanaka, *Langmuir*, 2002, **18**, 3226.

74 L. Yiping, G. C. Hadjipanayis, C. M. Sorensen and K. J. Klabunde, *J. Appl. Phys.*, 1994, **75**, 5885.

75 M. Heemeier, A. F. Carlsson, M. Naschitzki, M. Schmal, M. Baumer and H.-J. Freund, *Angew. Chem., Int. Ed.*, 2002, **41**, 4073.

76 B. Stahl, J. Ellrich, R. Theissmann, M. Ghafari, S. Bhattacharya, H. Hahn, N. S. Gajbhiye, D. Kramer, R. N. Viswanath, J. Weissmuller and H. Gleiter, *Phys. Rev. B: Condens. Matter Mater. Phys.*, 2003, **67**, 014422.

77 A. C. C. Yu, M. Mizuno, Y. Sasaki, M. Inoue, H. Kondo, I. Ohta, D. Djayaprawira and M. Takahashi, *Appl. Phys. Lett.*, 2003, **82**, 4352.

78 C. N. Chinnasamy, B. Jeyadevan, K. Shinoda and K. Tohji, *J. Appl. Phys.*, 2003, **93**, 7583.

79 M. L. Rao and S. S. Manoharan, *Solid State Commun.*, 2004, **129**, 781.

80 M. Chen and D. E. Nikles, *Nano Lett.*, 2002, **2**, 211.

81 D. Zitoun, C. Amiens, B. Chaudret, M. C. Fromen, P. Lecante, M. J. Casanove and M. Respaud, *J. Phys. Chem. B*, 2003, **107**, 6997.

82 C. Damle and M. Sastry, *J. Mater. Chem.*, 2002, **12**, 1860.

83 L. Yue, R. Sabiryanov, E. M. Kirkpatrick and D. L. Leslie-Pelecky, *Phys. Rev. B: Condens. Matter Mater. Phys.*, 2000, **62**, 8969.

84 K. Kosugi, M. J. Bushiri and N. Nishi, *Appl. Phys. Lett.*, 2004, **84**, 1753.

85 S. I. Nikitenko, Y. Koltypin, V. Markovich, E. Rozenberg, G. Gorodetsky and A. Gedanken, *IEEE Trans. Magn.*, 2002, **38**, 2592.

86 S. I. Nikitenko, Y. Koltypin, O. Palchik, I. Felner, X. N. Xu and A. Gedanken, *Angew. Chem., Int. Ed.*, 2001, **40**, 4447.

87 J. Jiao and S. Seraphin, *J. Appl. Phys.*, 1998, **83**, 2442.

88 M. E. McHenry, S. A. Majetich, J. O. Artman, M. DeGraef and S. W. Staley, *Phys. Rev. B: Condens. Matter Mater. Phys.*, 1994, **49**, 11358.

89 B. H. Liu, J. Ding, Z. Y. Zhong, Z. L. Dong, T. White and J. Y. Lin, *Chem. Phys. Lett.*, 2002, **358**, 96.

90 E. Flahaut, F. Agnoli, J. Sloan, C. O'Connor and M. L. H. Green, *Chem. Mater.*, 2002, **14**, 2553.

91 Z.-J. Liu, Z.-Y. Yuan, W. Zhou, Z. Xu and L.-M. Peng, *Chem. Vap. Deposition*, 2001, **7**, 248.

92 J. Jiao and S. Seraphin, *Proc. - Electrochem. Soc.*, 1996, **96-10**, 688.

93 R. Seshadri, R. Sen, G. N. Subbanna, K. R. Kannan and C. N. R. Rao, *Chem. Phys. Lett.*, 1994, **231**, 308.

94 Y. D. Zhang, J. I. Budnick, W. A. Hines, S. A. Majetich and E. M. Kirkpatrick, *Appl. Phys. Lett.*, 2000, **76**, 94.

95 J. Ling, Y. Liu, G. Hao and X. Zhang, *Mater. Sci. Eng., B*, 2003, **100**, 186.

96 S. A. Majetich, J. O. Artman, M. E. McHenry, N. T. Nuhfer and S. W. Staley, *Phys. Rev. B: Condens. Matter Mater. Phys.*, 1993, **48**, 16845.

97 S. Seraphin, C. Beeli, J. M. Bonard, J. Jiao, P. A. Stadelmann and A. Chatelain, *J. Mater. Res.*, 1999, **14**, 2861.

98 J. J. Host, J. A. Block, K. Parvin, V. P. Dravid, J. L. Alpers, T. Sezen and R. LaDuca, *J. Appl. Phys.*, 1998, **83**, 793.

99 Y. Koltypin, A. Fernandez, T. C. Rojas, J. Campora, P. Palma, R. Prozorov and A. Gedanken, *Chem. Mater.*, 1999, **11**, 1331.

100 T. C. Rojas, M. J. Sayagues, A. Caballero, Y. Koltypin, A. Gedanken, L. Ponsonnet, B. Vacher, J. M. Martin and A. Fernandez, *J. Mater. Chem.*, 2000, **10**, 715.

101 P. B. Oliete, T. C. Rojas, A. Fernandez, A. Gedanken, Y. Koltypin and F. Palacio, *Acta Mater.*, 2004, **52**, 2165.

102 P.-Z. Si, Z.-D. Zhang, D.-Y. Geng, C.-Y. You, X.-G. Zhao and W.-S. Zhang, *Carbon*, 2003, **41**, 247.

103 X.-C. Sun and X.-L. Dong, *Mater. Res. Bull.*, 2002, **37**, 991.

104 V. P. Dravid, J. J. Host, M. H. Teng, B. Elliott, J. Hwang, D. L. Johnson, T. O. Mason and J. R. Weertman, *Nature*, 1995, **374**, 602.

105 Z. Guo, S. Park, H. T. Hahn, S. Wei, M. Moldovan, A. B. Karki and D. P. Young, *Appl. Phys. Lett.*, 2007, **90**, 053111.

106 Z. Guo, H. T. Hahn, H. Lin, A. B. Karki and D. P. Young, *J. Appl. Phys.*, 2008, **104**, 014314.

107 D. Zhang, S. Wei, D. P. Young and Z. Guo, *Nanoscale*, 2010, **2**, 917.

108 J. Zhu, S. Wei, D. Rutman, N. Haldolaarachchige, D. P. Young and Z. Guo, *Polymer*, 2011, **52**, 2947.

109 M. Z. Wu, Y. D. Zhang, S. Hui, T. D. Xiao, S. H. Ge, W. A. Hines and J. I. Budnick, *J. Appl. Phys.*, 2002, **92**, 491.

110 Y. Kobayashi, M. Horie, M. Konno, B. Rodriguez-Gonzalez and L. M. Liz-Marzan, *J. Phys. Chem. B*, 2003, **107**, 7420.

111 M. Wu, Y. D. Zhang, S. Hui, T. D. Xiao, S. Ge, W. A. Hines and J. I. Budnick, *J. Magn. Magn. Mater.*, 2004, **268**, 20.

112 S. Hui, M. Wu, S. Ge, D. Yan, Y. D. Zhang, T. D. Xiao, M. J. Yacaman, M. M. Yoshida, W. A. Hines and J. I. Budnick, *Mater. Res. Soc. Symp. Proc.*, 2002, **755**, 159.

113 J. Zhu, S. Wei, N. Haldolaarachchige, D. P. Young and Z. Guo, *J. Phys. Chem. C*, 2011, **115**, 15304.

114 M. Z. Wu, Y. D. Zhang, S. Hui, T. D. Xiao, S. H. Ge, W. A. Hines, J. I. Budnick and M. J. Yacaman, *J. Appl. Phys.*, 2002, **92**, 6809.

115 S. Hui, Y. D. Zhang, T. D. Xiao, M. Wu, S. Ge, W. A. Hines, J. I. Budnick, M. J. Yacaman and H. E. Troiani, *Mater. Res. Soc. Symp. Proc.*, 2002, **703**, 237.

116 W. Zhao, J. Gu, L. Zhang, H. Chen and J. Shi, *J. Am. Chem. Soc.*, 2005, **127**, 8916.

117 M. Wu, Y. D. Zhang, S. Hui and S. Ge, *Mater. Res. Soc. Symp. Proc.*, 2002, **755**, 147.

118 K. Sakiyama, K. Koga, T. Seto, M. Hirasawa and T. Orii, *J. Phys. Chem. B*, 2004, **108**, 523.

119 G. S. Chaubey and J. Kim, *Bull. Korean Chem. Soc.*, 2007, **28**, 2279.

120 E. E. Carpenter, S. Calvin, R. M. Stroud and V. G. Harris, *Chem. Mater.*, 2003, **15**, 3245–3246.

121 K. Fauth, E. Goering, G. Schutz and L. T. Kuhn, *J. Appl. Phys.*, 2004, **96**, 399–403.

122 E. E. Carpenter, A. Kumbhar, J. A. Wiemann, H. Srikanth, J. Wiggins, W. Zhou and C. J. O'Connor, *Mater. Sci. Eng., A*, 2000, **286**, 81.

123 B. Ravel, E. E. Carpenter and V. G. Harris, *J. Appl. Phys.*, 2002, **91**, 8195–8197.

124 M. Chen, S. Yamamuro, D. Farrell and S. A. Majetich, *J. Appl. Phys.*, 2003, **93**, 7551–7553.

125 J. Lin, W. Zhou, A. Kumbhar, J. Wiemann, J. Fang, E. E. Carpenter and C. J. O'Connor, *J. Solid State Chem.*, 2001, **159**, 26.

126 W. L. Zhou, E. E. Carpenter, J. Lin, A. Kumbhar, J. Sims and C. J. O'Connor, *Eur. Phys. J. D*, 2001, **16**, 289.

127 D. A. Fleming, M. Napolitano and M. E. Williams, *Mater. Res. Soc. Symp. Proc.*, 2003, **746**, 207.

128 E. E. Carpenter, C. Sangregorio and C. J. O'Connor, *IEEE Trans. Magn.*, 1999, **35**, 3496.

129 Z. Lu, M. D. Prouty, Z. Guo, V. O. Golub, C. S. S. R. Kumar and Y. M. Lvov, *Langmuir*, 2005, **21**, 2042–2050.

130 Z. Guo, M. Moldovan, D. P. Young, L. L. Henry and E. J. Podlaha, *Electrochem. Solid-State Lett.*, 2007, **10**, E31.

131 J.-I. Park and J. Cheon, *J. Am. Chem. Soc.*, 2001, **123**, 5743.

132 S. U. Son, Y. Jang, J. Park, H. B. Na, H. M. Park, H. J. Yun, J. Lee and T. Hyeon, *J. Am. Chem. Soc.*, 2004, **126**, 5026.

133 S. Sao-Joao, S. Giorgio, J. M. Penisson, C. Chapon, S. Bourgeois and C. Henry, *J. Phys. Chem. B*, 2005, **109**, 342.

134 Z. Guo, C. S. S. R. Kumar, L. L. Henry, E. E. Doomes, J. Hormes and E. J. Podlaha, *J. Electrochem. Soc.*, 2005, **152**, D1.

135 A. J. García-Bastida, R. D. Sánchez, J. García-Otero, José Rivas, A. González-Penedo, J. Solla and M. A. López-Quintela, *Materials Science Forum*, 1998, **269-272**, 919.

136 O. Crisan, M. Angelakeris, N. K. Flevaris and G. Filoti, *J. Optoelectron. Adv. Mater.*, 2003, **5**, 959.

137 N. A. D. Burke, H. D. H. Stoever and F. P. Dawson, *Chem. Mater.*, 2002, **14**, 4752.

138 H. Kim, M. Achermann, L. P. Balet, J. A. Hollingsworth and V. I. Klimov, *J. Am. Chem. Soc.*, 2005, **127**, 544.

139 B. L. Cushing, V. L. Kolesnichenko and C. J. O'Connor, *Chem. Rev.*, 2004, **104**, 3893.

140 A.-H. Lu, E. L. Salabas and F. Schueth, *Angew. Chem., Int. Ed.*, 2007, **46**, 1222.

141 W. Schartl, *Nanoscale*, 2010, **2**, 829–843.

142 J. Tanori, N. Duxin, C. Petit, I. Lisiecki, P. Veillet and M. P. Pileni, *Colloid Polym. Sci.*, 1995, **273**, 886.

143 C. Petit, A. Taleb and M. P. Pileni, *Adv. Mater.*, 1998, **10**, 259.

144 K. J. Klabunde, D. Zhang, G. N. Glavee, C. M. Sorensen and G. C. Hadjipanayis, *Chem. Mater.*, 1994, **6**, 784.

145 N. Duxin, O. Stephan, C. Petit, P. Bonville, C. Colliex and M. P. Pileni, *Chem. Mater.*, 1997, **9**, 2096.

146 B. Bonnemain, *J. Drug Targeting*, 1998, **6**, 167.

147 E. E. Carpenter, J. A. Sims, J. A. Wienmann, W. L. Zhou and C. J. O'Connor, *J. Appl. Phys.*, 2000, **87**, 5615.

148 G. Salazar-Alvarez, M. Mikhailova, M. Toprak, Y. Zhang and M. Muhammed, *Mater. Res. Soc. Symp. Proc.*, 2002, **707**, 263.

149 N. S. Sobal, U. Ebels, H. Moehwald and M. Giersig, *J. Phys. Chem. B*, 2003, **107**, 7351.

150 Y. Yin, R. M. Rioux, C. K. Erdonmez, S. Hughes, G. A. Somorjai and A. P. Alivisatos, *Science*, 2004, **304**, 711.

151 J. M. Buriak, *Science*, 2004, **304**, 692.

152 E. J. Podlaha, *Nano Lett.*, 2001, **1**, 413.

153 Z. Xu, Y. Hou and S. Sun, *J. Am. Chem. Soc.*, 2007, **129**, 8698.

154 S. Seraphin, D. Zhou, J. Jiao, J. C. Withers and R. Loutfy, *Appl. Phys. Lett.*, 1993, **63**, 2073.

155 E. M. Brunsman, R. Sutton, E. Bortz, S. Kirkpatrick, K. Midelfort, J. Williams, P. Smith, M. E. McHenry and S. A. Majetich, *et al.*, *J. Appl. Phys.*, 1994, **75**, 5882.

156 V. Skumryev, S. Stoyanov, Y. Zhang, G. Hadjipanayis, D. Givord and J. Nogues, *Nature*, 2003, **423**, 850.

157 H. Bi, S. Li, X. Jiang, Y. Du and C. Yang, *Phys. Lett. A*, 2003, **307**, 69.

158 D. L. Peng, K. Sumiyama, T. J. Konno, T. Hihara and S. Yamamuro, *Phys. Rev. B: Condens. Matter Mater. Phys.*, 1999, **60**, 2093.

159 H. Wen, R. K. Zheng, K. K. Fung and X. X. Zhang, *J. Magn. Magn. Mater.*, 2004, **270**, 407.

160 Y. Wang, X. Teng, J.-S. Wang and H. Yang, *Nano Lett.*, 2003, **3**, 789–793.

161 K. J. Klabunde, *Nanoscale Materials in Chemistry*, Wiley-Interscience, New York, 2001.

162 V. Salgueirino-Maceira, F. Caruso and L. M. Liz-Marzan, *J. Phys. Chem. B*, 2003, **107**, 10990.

163 J. L. West, N. J. Halas, S. J. Oldenburg and R. D. Averitt, *Metal Nanoshells for Biosensing Applications*, US Pat. 2000-616154, 6699724, Wm. Marsh Rice University, US Ser No 38,377, p. 20.

164 Y. Hu, L. He and Y. Yin, *Angew. Chem., Int. Ed.*, 2011, **50**, 3747.

165 J. Ge, Y. Hu, T. Zhang, T. Huynh and Y. Yin, *Langmuir*, 2008, **24**, 3671.

166 J. Ge, Y. Hu, M. Biasini, W. P. Beyermann and Y. Yin, *Angew. Chem., Int. Ed.*, 2007, **46**, 4342.

167 J. Ge, Y. Hu and Y. Yin, *Angew. Chem., Int. Ed.*, 2007, **46**, 7248.

168 J. Ge, S. Kwon and Y. Yin, *J. Mater. Chem.*, 2010, **20**, 5777.

169 Y. Hu, L. He and Y. Yin, *Angew. Chem., Int. Ed.*, 2011, **50**, 3747.

170 J. Ge, L. He, J. Goebl and Y. Yin, *J. Am. Chem. Soc.*, 2009, **131**, 3484.

171 A. H. Lu, E. L. Salabas and F. Schuth, *Angew. Chem., Int. Ed.*, 2007, **119**, 1242.

172 M. Ye, Q. Zhang, Y. Hu, J. Ge, Z. Lu, L. He, Z. Chen and Y. Yin, *Chem.–Eur. J.*, 2010, **16**, 6243.

173 R. Xuan, Q. Wu, Y. Yin and J. Ge, *J. Mater. Chem.*, 2011, **21**, 3672.

174 M. Ye, S. Zorba, L. He, Y. Hu, R. T. Maxwell, C. Farah, Q. Zhang and Y. Yin, *J. Mater. Chem.*, 2010, **20**, 7965.

175 S. Zorba, R. T. Maxwell, C. Farah, L. He, M. Ye and Y. Yin, *J. Phys. Chem. C*, 2010, **114**, 17868.

176 J. Fang, J. He, E. Y. Shin, D. Grimm, C. J. O'Connor and M.-J. Jun, *Mater. Res. Soc. Symp. Proc.*, 2003, **774**, 149.

177 Q. Zhang, J. Ge, J. Goebl, Y. Hu, Y. Sun and Y. Yin, *Adv. Mater.*, 2010, **22**, 1905.

178 L. Y. Wang, J. Luo, Q. Fan, M. Suzuki, I. S. Suzuki, M. H. Engelhard, Y. H. Lin, N. Kim, J. Q. Wang and C. J. Zhong, *J. Phys. Chem. B*, 2005, **109**, 21593.

179 L. R. Hirsch, J. B. Jackson, A. Lee, N. J. Halas and J. West, *Anal. Chem.*, 2003, **75**, 2377.

180 L. Y. Wang, J. W. Bai, Y. J. Li and Y. Huang, *Angew. Chem., Int. Ed.*, 2008, **47**, 2439.

181 J. B. Jackson, S. L. Westcott, L. R. Hirsch, J. L. West and N. J. Halas, *Appl. Phys. Lett.*, 2003, **82**, 257.

182 Z. Guo, S. Park, H. T. Hahn, S. Wei, M. Moldovan, A. B. Karki and D. P. Young, *J. Appl. Phys.*, 2007, **101**, 09M511.

183 Z. Guo, S. E. Lee, H. Kim, S. Park, H. T. Hahn, A. B. Karki and D. P. Young, *Acta Mater.*, 2009, **57**, 267.

184 S. W. Phang and N. Kuramoto, *Polym. Compos.*, 2010, **31**, 516.

185 S. Xiao, M. Shen, R. Guo, S. Wang and X. Shi, *J. Phys. Chem. C*, 2009, **113**, 18062.

186 D. W. Elliott, H.-L. Lien and W.-x. Zhang, *J. Environ. Qual.*, 2008, **37**, 2192.

187 J. T. Nurmi, P. G. Tratnyek, V. Sarathy, D. R. Baer, J. E. Amonette, K. Pecher, C. Wang, J. C. Linehan, D. W. Matson, R. L. Penn and M. D. Driessen, *Environ. Sci. Technol.*, 2005, **39**, 1221.

188 D. L. Peng, K. Sumiyama, T. Hihara, S. Yamamuro and T. J. Konno, *Phys. Rev. B: Condens. Matter Mater. Phys.*, 2000, **61**, 3103.

189 L. Del Bianco, D. Fiorani, A. M. Testa, E. Bonetti, L. Savini and S. Signoretti, *Phys. Rev. B: Condens. Matter Mater. Phys.*, 2002, **66**, 174418.

190 F. Luis, J. M. Torres, L. M. Garcia, J. Bartolome, J. Stankiewicz, F. Petroff, F. Fettar, J. L. Maurice and A. Vaures, *Phys. Rev. B: Condens. Matter Mater. Phys.*, 2002, **65**, 094409.

191 Z. Guo, K. Lei, Y. Li, H. W. Ng and H. T. Hahn, *Compos. Sci. Technol.*, 2008, **68**, 1513.

192 D. Zhang, A. B. Karki, D. Rutman, D. P. Young, A. Wang, D. Cocke, T. H. Ho and Z. Guo, *Polymer*, 2009, **50**, 4189.

193 B. D. Cullity, *Introduction to Magnetic Materials*, Addision-Wesley, Reading, MA, 1972.

194 D. Zhang, K. J. Klabunde, C. M. Sorensen and G. C. Hadjipanayis, *Phys. Rev. B: Condens. Matter Mater. Phys.*, 1998, **58**, 14167.

195 D. Kechrakos and K. N. Trohidou, *Phys. Rev. B: Condens. Matter Mater. Phys.*, 1998, **58**, 12169.

196 J. Guevara, A. M. Llois and M. Weissmann, *Phys. Rev. Lett.*, 1998, **81**, 5306.

197 B. Wang, X. Chen, G. Chen, G. Wang and J. Zhao, *Surf. Rev. Lett.*, 2004, **11**, 15.

198 Z. Guo, L. L. Henry and E. J. Podlaha, *ECS Trans.*, 2006, **1**, 63.

199 Z. Guo, L. L. Henry and E. J. Podlaha, *ECS Trans.*, 2007, **3**, 337.

200 Z. Guo, C. Kumar, L. Henry, J. Hormes and E. J. Podlaha, Abstracts in the 205th ECS Meeting, 2004, **MA2004-01**, A1-23.

201 J. Jiao, S. Seraphin, X. Wang and J. C. Withers, *J. Appl. Phys.*, 1996, **80**, 103–108.

202 Y. Mizukoshi, T. Fujimoto, Y. Nagata, R. Oshima and Y. Maeda, *J. Phys. Chem. B*, 2000, **104**, 6028.

203 X. Teng and H. Yang, *J. Am. Chem. Soc.*, 2003, **125**, 14559.

204 D. L. Peng, T. Asai, N. Nozawa, T. Hihara and K. Sumiyama, *Appl. Phys. Lett.*, 2002, **81**, 4598.

205 J. Wong, F. W. Lytle, R. P. Messmer and D. H. Maylotte, *Phys. Rev. B: Condens. Matter Mater. Phys.*, 1984, **30**, 5596.

206 P. Behrens, *TrAC, Trends Anal. Chem.*, 1992, **11**, 237.

207 L. X. Chen, T. Rajh, Z. Wang and M. C. Thurnauer, *J. Phys. Chem. B*, 1997, **101**, 10688.

208 L. X. Chen, Z. Wang, J. K. Burdett, P. A. Montano and J. R. Norris, *J. Phys. Chem.*, 1995, **99**, 7958.

209 H. Modrow, S. Bucher, J. Hormes, R. Brinkmann and H. Boennemann, *J. Phys. Chem. B*, 2003, **107**, 3684.

210 J. Rothe, J. Hormes, H. Boennemann, W. Brijoux and K. Siepen, *J. Am. Chem. Soc.*, 1998, **120**, 6019.

211 G. A. Somorjai, *Appl. Surf. Sci.*, 1997, **121/122**, 1.

212 C.-W. Chen and M. Akashi, *Langmuir*, 1997, **13**, 6465.

213 M. Sasaki, M. Osada, N. Higashimoto, T. Yamamoto, A. Fukuoka and M. Ichikawa, *J. Mol. Catal. A: Chem.*, 1999, **141**, 223.

214 M. T. Reetz and E. Westermann, *Angew. Chem., Int. Ed.*, 2000, **39**, 165.

215 E. H. Rahim, F. S. Kamounah, J. Frederiksen and J. B. Christensen, *Nano Lett.*, 2001, **1**, 499.

216 S.-W. Kim, M. Kim, W. Y. Lee and T. Hyeon, *J. Am. Chem. Soc.*, 2002, **124**, 7642.

217 V. Kogan, Z. Aizenshtat, R. Popovitz-Biro and R. Neumann, *Org. Lett.*, 2002, **4**, 3529.

218 J. Huang, T. Jiang, H. Gao, B. Han, Z. Liu, W. Wu, Y. Chang and G. Zhao, *Angew. Chem., Int. Ed.*, 2004, **43**, 1397.

219 R. Narayanan and M. A. El-Sayed, *J. Phys. Chem. B*, 2003, **107**, 12416.

220 K. M. Kang, H. W. Kim, I. W. Shim and H. Y. Kwak, *Fuel Process. Technol.*, 2011, **92**, 1236.

221 S. H. Joo, J. Y. Park, C.-K. Tsung, Y. Yamada, P. Yang and G. A. Somorjai, *Nat. Mater.*, 2009, **8**, 126.

222 J. C. Park, H. J. Lee, J. Y. Kim, K. H. Park and H. Song, *J. Phys. Chem. C*, 2010, **114**, 6381.

223 J. C. Park, J. U. Bang, J. Lee, C. H. Ko and H. Song, *J. Mater. Chem.*, 2010, **20**, 1239.

224 R. Guttel, M. Paul and F. Schuth, *Chem. Commun.*, 2010, **46**, 895.

225 A. D. Pandey, R. Guttel, M. Leoni, F. Schuth and C. Weidenthaler, *J. Phys. Chem. C*, 2010, **114**, 19386.

226 M. Feyen, C. Weidenthaler, R. Guttel, K. Schlichte, U. Holle, A. H. Lu and F. Schuth, *Chem.–Eur. J.*, 2011, **17**, 598.

227 H. J. Hah, J. I. Um, S. H. Han and S. M. Koo, *Chem. Commun.*, 2004, 1012.

228 J. Y. Kim, S. B. Yoon and J. S. Yu, *Chem. Commun.*, 2003, 790.

229 M. Kim, K. Sohn, H. B. Na and T. Hyeon, *Nano Lett.*, 2002, **2**, 1383.

230 J. Ge, Q. Zhang, T. Zhang and Y. Yin, *Angew. Chem., Int. Ed.*, 2008, **47**, 8924.

231 Q. J. Ge, Y. M. Huang, F. Y. Qiu and S. B. Li, *Appl. Catal., A*, 1998, **167**, 23.

232 J. Bao, J. He, Y. Zhang, Y. Yoneyama and N. Tsubaki, *Angew. Chem., Int. Ed.*, 2008, **47**, 353.

233 G. Yang, M. Thongkam, T. Vitidsant, Y. Yoneyama, Y. Tan and N. Tsubaki, *Catal. Today*, 2011, **171**, 229.

234 M. Jakob, H. Levanon and P. V. Kamat, *Nano Lett.*, 2003, **3**, 353.

235 V. Subramanian, E. E. Wolf and P. V. Kamat, *J. Am. Chem. Soc.*, 2004, **126**, 4943.

236 V. Subramanian, E. Wolf and P. V. Kamat, *J. Phys. Chem. B*, 2001, **105**, 11439.

237 V. Subramanian, E. E. Wolf and P. V. Kamat, *Langmuir*, 2003, **19**, 469.

238 T. Hirakawa and P. V. Kamat, *J. Am. Chem. Soc.*, 2005, **127**, 3928.

239 M. N. Baibich, J. M. Broto, A. Fert, F. N. Van Dau, F. Petroff, P. Etienne, G. Creuzet, A. Friederich and J. Chazelas, *Phys. Rev. Lett.*, 1988, **61**, 2472.

240 G. Binasch, P. Grünberg, F. Saurenbach and W. Zinn, *Phys. Rev. B: Condens. Matter Mater. Phys.*, 1989, **39**, 4828.

241 *The Nobel Prize in Physics*, 2007, http://nobelprize.org/nobel_prizes/physics/laureates/2007/press.html.

242 G. A. Prinz, *Science*, 1998, **282**, 1660.

243 M. Freeman, *Phys. Teach.*, 2009, **47**, 206.

244 W. P. McCray, *Nat. Nanotechnol.*, 2009, **4**, 2.

245 J. S. Murday, *J. Nanopart. Res.*, 1999, **1**, 501.

246 C. P. O. Treutler, *Sens. Actuators, A*, 2001, **91**, 2.

247 C. Giebeler, D. J. Adelerhof, A. E. T. Kuiper, J. B. A. van Zon, D. Oelgeschlager and G. Schulz, *Sens. Actuators, A*, 2001, **91**, 16.

248 P. P. Freitas, J. L. Costa, N. Almeida, L. V. Melo, F. Silva, J. Bernardo and C. Santos, *Proceedings of AIP*, 1999, p. 5459.

249 P. R. Downey and A. B. Flatau, *Proceeding of the 49th Annual Conference on Magnetism and Magnetic Materials*, AIP, Jacksonville, Florida (USA), 2005, 10R505-503.

250 M. M. Miller, G. A. Prinz, P. Lubitz, L. Hoines, J. J. Krebs, S. F. Cheng and F. G. Parsons, *Proceeding of The 41st Annual Conference on Magnetism and Magnetic Materials*, AIP, Atlanta, Georgia (USA), 1997, p. 4284.

251 K. Kapser, S. Zaruba, P. Slama and E. Katzmaier, *Proceeding of Advanced Microsystems for Automotive Applications 2008*, 2008, pp. 211–227.

252 M. N. Baibich, J. M. Broto, A. Fert, F. Nguyen Van Dau, F. Petroff, P. Eitenne, G. Creuzet, A. Friederich and J. Chazelas, *Phys. Rev. Lett.*, 1988, **61**, 2472.

253 A. E. Berkowitz, J. R. Mitchell, M. J. Carey, A. P. Young, S. Zhang, F. E. Spada, F. T. Parker, A. Hutten and G. Thomas, *Phys. Rev. Lett.*, 1992, **68**, 3745.

254 P. Xiong, G. Xiao, J. Q. Wang, J. Q. Xiao, J. S. Jiang and C. L. Chien, *Phys. Rev. Lett.*, 1992, **69**, 3220.

255 H. Zhang, in *Mechanical Engineering*, Louisiana State University, Baton Rogue, 1999.

256 S. Tumanski, *Thin film Magnetoresistive Sensors*, Institute of Physics Pub, Bristol, Philadelphia, 2001.

257 A. Hutten, D. Sudfeld, K. Wojczykowski, P. Jutzi and G. Reiss, *J. Magn. Magn. Mater.*, 2003, **262**, 23.

258 S. S. P. Parkin, *Annu. Rev. Mater. Sci.*, 1995, **25**, 357.

259 J. Q. Xiao, J. S. Jiang and C. L. Chien, *Phys. Rev. Lett.*, 1992, **68**, 3749.

260 C. L. Chien, *Annu. Rev. Mater. Sci.*, 1995, **25**, 129.

261 J. Q. Wang and G. Xiao, *Phys. Rev. B: Condens. Matter Mater. Phys.*, 1994, **49**, 3982.

262 S. S. P. Parkin, R. F. C. Farrow, T. A. Rabedeau, R. F. Marks, G. R. Harp, Q. Lam, C. Chappert, M. F. Toney, R. Savoy and R. Geiss, *Europhys. Lett.*, 1993, **22**, 455.

263 M. Y. Zhuravlev, H. O. Lutz and A. V. Vedyayev, *Phys. Rev. B: Condens. Matter Mater. Phys.*, 2001, **6317**, 174409.

264 A. E. Berkowitz, J. R. Mitchell, M. J. Carey, A. P. Young, D. Rao, A. Starr, S. Zhang, F. E. Spada, F. T. Parker, A. Hutten and G. Thomas, *J. Appl. Phys.*, 1993, **73**, 5320.

265 S.-J. Cho, S. M. Kauzlarich, J. Olamit, K. Liu, F. Grandjean, L. Rebbouh and G. J. Long, *J. Appl. Phys.*, 2004, **95**, 6804.

266 L. Savini, E. Bonetti, L. Del Bianco, L. Pasquini, S. Signoretti, P. Allia, M. Coisson, J. Moya, V. Selvaggini, P. Tiberto and F. Vinai, *J. Appl. Phys.*, 2002, **91**, 8593.

267 L. J. Deng and M. G. Han, *Appl. Phys. Lett.*, 2007, **91**, 023119.

268 C. L. Zhu, M. L. Zhang, Y. J. Qiao, G. Xiao, F. Zhang and Y. J. Chen, *J. Phys. Chem. C*, 2010, **114**, 16229.

269 R. Che, L. M. Peng, X. Duan, Q. Chen and X. Liang, *Adv. Mater.*, 2004, **16**, 401.

270 Y. D. Deng, L. N. Li, B. Shen, L. Liu and W. B. Hu, *J. Appl. Phys.*, 2006, **100**, 014304.

271 C. Wang, X. J. Han, X. L. Zhang, S. R. Hu, T. Zhang, J. Y. Wang, Y. C. Du, X. H. Wang and P. Xu, *J. Phys. Chem. C*, 2010, **114**, 14826.

272 M. Wu, Y. D. Zhang, S. Hui, T. D. Xiao, S. Ge, W. A. Hines, J. I. Budnick and G. W. Taylor, *Appl. Phys. Lett.*, 2002, **80**, 4404.

273 X. G. Liu, D. Y. Geng, H. Meng, P. J. Shang and Z. D. Zhang, *Appl. Phys. Lett.*, 2008, **92**, 173117.

274 S. Sugimoto, T. Maeda, D. Book, T. Kagotani, K. Inomata, M. Homma, H. Ota, Y. Houjou and R. Sato, *J. Alloys Compd.*, 2002, **330**, 301.

275 J. R. Liu, M. Itoh and K. Machida, *Chem. Lett.*, 2003, **32**, 394.

276 J. R. Liu, M. Itoh and K. Machida, *Appl. Phys. Lett.*, 2003, **83**, 4017.

277 P. Xu, X. J. Han, C. Wang, D. H. Zhou, Z. S. Lv, A. H. Wen, X. H. Wang and B. Zhang, *J. Phys. Chem. B*, 2008, **112**, 10443.

278 M. S. Cao, X. L. Shi, X. Y. Fang, H. B. Jin, Z. L. Hou, W. Zhou and Y. J. Chen, *Appl. Phys. Lett.*, 2007, **91**, 203110.

279 J. R. Liu, M. Itoh and K. Machida, *Appl. Phys. Lett.*, 2006, **88**, 062503.

280 R. C. Che, C. Y. Zhi, C. Y. Liang and X. G. Zhou, *Appl. Phys. Lett.*, 2006, **88**, 033105.

281 A. Wadhawan, D. Garrett and J. M. Perez, *Appl. Phys. Lett.*, 2003, **83**, 2683.
282 B. Wen, J. J. Zhao, Y. P. Duan, X. G. Zhang, Y. B. Zhao, C. Dong, S. H. Liu and T. J. Li, *J. Phys. D: Appl. Phys.*, 2006, **39**, 1960.
283 X. F. Zhang, X. L. Dong, H. Huang, Y. Y. Liu, W. N. Wang, X. G. Zhu, B. Lv, J. P. Lei and C. G. Lee, *Appl. Phys. Lett.*, 2006, **89**, 053115.
284 X. Liu, Z. Zhang and Y. Wu, *Composites, Part B*, 2011, **42**, 326.
285 Z. W. Zhou, S. K. Liu and L. X. Gu, *J. Appl. Polym. Sci.*, 2001, **80**, 1520.
286 Y. J. Chen, M. S. Cao, T. H. Wang and Q. Wan, *Appl. Phys. Lett.*, 2004, **84**, 3367.
287 S. J. Yan, L. Zhen, C. Y. Xu, J. T. Jiang and W. Z. Shao, *J. Phys. D: Appl. Phys.*, 2010, **43**, 245003.
288 Y. P. Wu, Z. W. Li, L. F. Chen, S. J. Wang and C. K. Ong, *J. Appl. Phys.*, 2004, **95**, 4235.
289 X. Guo, Y. Deng, D. Gu, R. Che and D. Zhao, *J. Mater. Chem.*, 2009, **19**, 6706.
290 Y. Duan, S. Liu and H. Guan, *Sci. Technol. Adv. Mater.*, 2005, **6**, 513.
291 R. Faez, I. M. Martin, M. A. De Paoli and M. C. Rezende, *Synth. Met.*, 2001, **119**, 435.
292 D. A. Makeiff and T. Huber, *Synth. Met.*, 2006, **156**, 497.
293 S. W. Phang, M. Tadokoro, J. Watanabe and N. Kuramoto, *Synth. Met.*, 2008, **158**, 251.
294 Y. Li, G. Chen, Q. Li, G. Qiu and X. Liu, *J. Alloys Compd.*, 2011, **509**, 4104.
295 A. Ohlan, K. Singh, A. Chandra and S. K. Dhawan, *ACS Appl. Mater. Interfaces*, 2010, **2**, 927.
296 R. Hao, R. Xing, Z. Xu, Y. Hou, S. Gao and S. Sun, *Adv. Mater.*, 2010, **22**, 2729.
297 Z. Xu, C. Shen, Y. Hou, H. Gao and S. Sun, *Chem. Mater.*, 2009, **21**, 1778.
298 Y. Hou, Z. Xu and S. Sun, *Angew. Chem., Int. Ed.*, 2007, **46**, 6329.
299 L. Zhang, J. Wu, H. Liao, Y. Hou and S. Gao, *Chem. Commun.*, 2009, 4378.
300 C. Loo, A. Lin, L. Hirsch, M.-H. Lee, J. Barton, N. Halas, J. West and R. Drezek, *Technol. Cancer Res. Treat.*, 2004, **3**, 33.
301 J. Jang and H. Ha, *Chem. Mater.*, 2003, **15**, 2109.
302 O. P. Tiourina, A. A. Antipov, G. B. Sukhorukov, N. I. Larionova, Y. Lvov and H. Mohwald, *Macromol. Biosci.*, 2001, **1**, 209.
303 A. A. Antipov, G. B. Sukhorukov and H. Moehwald, *Langmuir*, 2003, **19**, 2444.
304 G. B. Sukhorukov, A. A. Antipov, A. Voigt, E. Donath and H. Mohwald, *Macromol. Rapid Commun.*, 2001, **22**, 44.
305 Y. Lvov, A. A. Antipov, A. Mamedov, H. Moehwald and G. B. Sukhorukov, *Nano Lett.*, 2001, **1**, 125.
306 I. L. Radtchenko, G. B. Sukhorukov and H. Mohwald, *Int. J. Pharm.*, 2002, **242**, 219.
307 M. Babincova, P. Cicmanec, V. Altanerova, C. Altaner and P. Babinec, *Bioelectrochemistry*, 2002, **55**, 17–19.
308 O. Saslawski, C. Weingarten, J. P. Benoit and P. Couvreur, *Life Sci.*, 1988, **42**, 1521–1528.
309 J. Kost, J. Wolfrum and R. Langer, *J. Biomed. Mater. Res.*, 1987, **21**, 1367.
310 G. Decher, *Science*, 1997, **277**, 1232.
311 Y. Lu, Y. Zhao, L. Yu, L. Dong, C. Shi, M. J. Hu, Y. J. Xu, L. P. Wen and S. H. Yu, *Adv. Mater.*, 2010, **22**, 1407.
312 D. Shao, K. Xu, X. Song, J. Hu, W. Yang and C. Wang, *J. Colloid Interface Sci.*, 2009, **336**, 526.
313 J. Gao, G. Liang, B. Zhang, Y. Kuang, X. Zhang and B. Xu, *J. Am. Chem. Soc.*, 2007, **129**, 1428.
314 J. Fei, Y. Cui, X. Yan, W. Qi, Y. Yang, K. Wang, Q. He and J. Li, *Adv. Mater.*, 2008, **20**, 452.
315 Y. Zhai, J. Zhai, M. Zhou and S. Dong, *J. Mater. Chem.*, 2009, **19**, 7030.
316 W. Cai, J. Yu, B. Cheng, B. L. Su and M. Jaroniec, *J. Phys. Chem. C*, 2009, **113**, 14739.
317 X. J. Tang, Y. Bai, A. Duong, M. T. Smith, L. Y. Li and L. P. Zhang, *Environ. Int.*, 2009, **35**, 1210.
318 J. Ji, P. Zenga, S. Ji, W. Yang, H. Liu and Y. Li, *Catal. Today*, 2010, **158**, 305.
319 S. Xuan, L. Hao, W. Jiang, X. Gong, Y. Hu and Z. Chen, *Nanotechnology*, 2007, **18**, 035602.
320 X.-W. Wei, G.-X. Zhu, C.-J. Xia and Y. Ye, *Nanotechnology*, 2006, **17**, 4307.
321 S. R. Rudge, T. L. Kurtz, C. R. Vessely, L. G. Catterall and D. L. Williamson, *Biomaterials*, 2000, **21**, 1411.
322 N.-H. HSU, S.-L. Wang, Y.-C. Lin, G. D. Sheng and J.-F. Lee, *Environ. Sci. Technol.*, 2011, **44**, 6202.
323 Y. Xu and D. Zhao, *Water Res.*, 2007, **41**, 2101.
324 Y. C. Sharma, B. Singh, A. Agrawal and C. H. Weng, *J. Hazard. Mater.*, 2008, **151**, 789.
325 Y. A. Aydin and N. D. Aksoy, *Chem. Eng. J.*, 2009, **151**, 188.
326 J. Hu, G. Chen and I. M. C. Lo, *Water Res.*, 2005, **39**, 4528.
327 M. Imamoglu and O. Tekir, *Desalination*, 2008, **228**, 108.
328 K. Kadirvelu, C. Faur-Brasquet and P. L. Cloirec, *Langmuir*, 2000, **16**, 8404.
329 J.-K. Yang, H.-J. Park, H.-D. Lee and S.-M. Lee, *Colloids Surf., A*, 2009, **337**, 154–158.
330 M. A. A. Zaini, R. Okayama and M. Machida, *J. Hazard. Mater.*, 2009, **170**, 1119.
331 S.-Y. Wang, M.-H. Tsai, S.-F. Lo and M.-J. Tsai, *Bioresour. Technol.*, 2008, **99**, 7027.
332 Z. Tu, Q. He, X. Chang, Z. Hu, R. Gao, L. Zhang and Z. Li, *Anal. Chim. Acta*, 2009, **649**, 252.
333 K. Pillay, E. M. Cukrowska and N. J. Coville, *J. Hazard. Mater.*, 2009, **166**, 1067.
334 Z. H. Sun, L. F. Wang, P. P. Liu, S. C. Wang, B. Sun, D. Z. Jiang and F.-S. Xiao, *Adv. Mater.*, 2006, **18**, 1968.
335 J. Lee and H. W. Walker, *Environ. Sci. Technol.*, 2006, **40**, 7336.
336 L. Kronberg and T. Vartiainen, *Mutat. Res.*, 1988, **206**, 177.
337 K. Y. L. Angeline, M. F. Phillip and E. P. Ellie, *Environ. Sci. Technol.*, 1995, **29**, 242.
338 Y. Deng, D. Qi, C. Deng, X. Zhang and D. Zhao, *J. Am. Chem. Soc.*, 2008, **130**, 28.